Materials Today Bio 37 (2026) 102918

Contents lists available at ScienceDirect

Materials Today Bio

journal homepage: www.journals.elsevier.com/materials-today-bio

Acidic phosphate microenvironment within calcium phosphate bone graft substitutes drives ectopic bone formation in mice

Y. Maazouz [a,*], F. El Harouni [a], J. Piot [a], N. Warfing [b], R. De Miguel [b], N. Döbelin [a], M. Bohner [a]

[a] RMS foundation, Robert Mathys Strasse 1, Bettlach, 2544, Switzerland
[b] Anapath Research, Hammerstrasse 49, Liestal, 4410, Switzerland

A B S T R A C T

Material-induced heterotopic ossification (MIHO) by calcium-phosphate (CaP) bone graft substitutes (BGS) is difficult to anticipate because pore architecture, surface microstructure, and interfacial chemistry are often altered simultaneously. We compared six CaP granule formulations using an in-depth physical and chemical characterization. This included properties like granule size, pore architecture, intragranular concavities, specific surface area and microporosity, phase analysis, and controlled solution exposures that emulate confined fluid in pores to quantify pH, phosphate, calcium, and Ca/P release. These in-vitro readouts were paired with an intramuscular mouse model assessed at 35 and 56 days (early/late ossification centers, spicule density, bone area fraction, and standard host-reaction scores). Rank-based statistics mapped predictors to outcomes. Across materials, MIHO was observed primarily when two domains aligned. Physically, curvature-rich intragranular macropores were positively associated with the initiation of ectopic bone, while micro/nano-textured surface area within those pores was associated with later consolidation. Chemically, the most MIHO-competent materials tended to exhibit a phosphate-rich, mildly acidic interfacial milieu under confined-liquid conditions; this signature—captured by increased phosphate, decreased pH, and a reduced Ca/P release ratio—showed the strongest correlations with late histomorphometric endpoints. Apparent "phase effects" may largely reflect the interfacial chemistry those phases produced rather than intrinsic rankings based on solubility. The data suggest a simple, actionable rule set: concave, well-interconnected pores and micro/nano texture may help localize and sustain an acidic phosphate microenvironment that may bias soft tissues toward ectopic ossification. Practically, measuring ΔpH, ΔPO_4, and Ca/P under confined-liquid conditions may provide candidate in-vitro surrogates for MIHO and a rational basis to design CaP grafts either to promote osteoinduction where desired or to avoid it where it is a risk.

1. Introduction

Substances that can induce bone formation in a soft tissue have been investigated as early as Introduction 1909 when Pearce et al. showed that phenol 95% solution could induce bone formation in the kidney of dogs [1]. However, Marshall R. Urist produced the most compelling studies addressing the subject starting in 1961 [2] and the following series of articles introducing the concept of osteoinduction [3–7]. Later on, Urist identified, and coined the term, bone morphogenetic proteins (BMP) as the sole substance responsible for triggering the ectopic bone formation [8]. The question: "Why substances like toxins or implanted materials such as metals, ceramics or polymers can induce bone formation in ectopic sites if BMP are responsible for it?" was therefore left unanswered for many years and is still debated. One particular observation that Urist and others had made in their studies is that mineralization sometimes occurred prior to ectopic bone formation [2,9,10]. In spite of this observation, mineralization was dismissed by Urist [5] and little to no effort was dedicated to rule out the possibility that mineralization was essential to ectopic bone formation. Notwithstanding, another field of study, interested in pathologic heterotopic ossification (HO) induced by trauma or immobilization, highlighted its importance prior to bone formation in soft tissues [11–13]. Linden made the link between in vivo mineralization/calcification of decalcified bone and dentin and the ectopic bone formation it induced in1975 [14]. Since then many other studies have evoked this link [15–22]. Recently, Bohner et al. proposed that mineralization can produce a sustained local ionic homeostatic imbalance (SLIHI) within the porosity of BGS [23–26] and that this SLIHI triggers HO.

Recent in-vitro studies have shown that reactive calcium-phosphate (CaP) bone-graft substitutes (BGS) can strongly disturb the ionic balance of standard cell-culture media or simulated body fluids, scavenging up to ≈40–50 % of the soluble Ca^{2+} pool while either consuming or, depending on the medium formulation and CaP-BGS, even releasing inorganic phosphate [25,27–29]; the same ion-exchange process is likely to take place in vivo at the implant–tissue interface and is now regarded as a key step in generating the sustained local ionic

* Corresponding author.
E-mail address: yassine.maazouz@rms-foundation.ch (Y. Maazouz).

https://doi.org/10.1016/j.mtbio.2026.102918
Received 17 December 2025; Received in revised form 5 February 2026; Accepted 9 February 2026
Available online 10 February 2026

Table 1
– Relevant ionic concentrations (expressed in mM) of the SBF used in the ISO standard 23317 and the SBF used in the present study as compared to blood.

	Na^+	K^+	Mg^{2+}	Ca^{2+}	Cl^-	HCO_3^-	HPO_4^{2-}	SO_4^{2-}
Blood [43]	142.0	5.0	1.5	2.5	103.0	27.0	1.0	0.5
ISO 23317 [42]	142.0	5.0	1.5	2.5	147.8	4.2	1.0	0.5
SBF-A	157.3			7.3	172.2			
SBF-B	165.7				157.6		4.2	
SBF	**161.5**			**3.6**	**164.9**		**2.1**	
Modified BSBF-A	157.3			7.3	172.2			
Modified BSBF-B	270.3				157.6	104.6	4.2	
Modified BSBF	**213.8**			**3.6**	**164.3**	**52.3**	**2.1**	

homeostatic imbalance that precedes material-induced osteoinduction [23,25,26,30]. Material-induced heterotopic ossification (MIHO) has been tested and observed successfully in a variety of animal models. Ectopic bone is formed by the implantation of CaP-BGSs most reliably in the paravertebral muscle of large animals such as dogs, pigs or goats [21, 31–34]. Nonetheless the resources needed for such studies has led to the development of murine models that that are as predictive as their large animal counterparts [22,35]. A murine model constitutes the basis of an ASTM (ASTM 2529-13, American Society for Testing and Materials) standard designed to test the inductive properties of demineralized bone matrix products [36]. The ASTM suggests the use of a nude mouse model that is relevant for DBM products to avoid a potential xenogenic immune response of rejection. In the case of the testing of CaP-BGS a nude mouse model is not necessary because the materials are synthetic. Among all murine strains, Friend virus B sensitive mice (FVB) have demonstrated to be the most reliable of all to form bone ectopically when implanted with calcium phosphate BGS [35].

The present study focuses on evidencing the link between in vitro measurements of the chemical changes induced by calcium phosphate based bone graft substitutes (BGS) in relevant fluids, and their ectopic bone formation in a FVB mice model of ectopic implantation based on the ASTM 2529 [36]. For this matter, 4 types of calcium phosphate granules featuring different chemical composition, macroscopic and microscopic structure as well as 2 commercial BGS were characterized physiochemically, measured for their chemical interaction with water and Simulated Body Fluids (SBF) and implanted for 35 and 56 days in the leg muscle of FVB mice. The present study is a direct evaluation and quantitative correlation of the relationship between the physical and chemical action of BGS and their MIHO capacity.

2. Materials and methods

2.1. Materials

Non-commercial prototypes (Test materials, TA) were provided by Mathys Ltd, no detail was provided about their synthesis or processing. Granules were provided sterile, packaged in double blisters and their sizes were comprised between 0.125 mm and 0.700 mm. The different test materials were labeled TA1, TA2, TA3, and TA4.

The commercial BGS references cyclOs (CN, Mathys Ltd) and MagnetOs (CP, Kuros Biosciences) were supplied from the company (CN, Mathys Ltd) or purchased from ordinary commercial channels.

2.2. Physico-chemical characterisation

Phase identification and composition was determined by X-ray powder diffraction. Three separate samples of each material were milled in isopropanol with a McCrone Mill and dried under an infrared light overnight. The resulting powder was pressed in polymer holders. A diffractometer (D8 Advance, Bruker) was used in a theta-theta setup with Ni-filtered Cu-Kα irradiation. Samples were measured between 4 and 80° (2θ). Phase composition was quantified using Rietveld refinement (Profex,http://profex.doebelin.org) [37]. Crystalline models for HA, β-TCP and α-TCP were taken from PDF# 01-074-0565 [38], PDF# 04–008-8714 [39], and PDF 00-009-0348 [40], respectively.

The specific surface area was determined by nitrogen adsorption using the BET model (Gemini 2360, Micromeritics). Granules were predried at 150 °C for 20 min. The specific surface area was determined in triplicates for each material.

The surface and bulk microstructure of the CaP-BGS was observed through field-emission scanning electron microscopy (FE-SEM). Samples were glued with carbon tape onto aluminum pins and coated with a 20 nm thick (CCU-010, Safematic) gold layer. For the determination of intragranular macroporosity, samples were embedded in epoxy resin, ground and polished. Subsequently they were sputtered with a 15 nm layer of carbon (CCU-010, Safematic). Samples were observed with a field emission scanning electron microscope (Sigma 300, Zeiss) with the secondary electron detector (surface) or the back scattered detector (cross sections). In this manuscript, we use pore-size terminology following common convention for ceramic bone graft substitutes rather than the IUPAC adsorption classification. Accordingly, pores were classified by equivalent diameter as micropores <10 μm and intragranular macropores ≥ 10 μm (i.e., pores above the 10 μm threshold were grouped as macroporosity for the purposes of this study). Topography was derived from SEM micrographs examining the size surface features, supra micrometric dominant surfaces were allocated the value of 0 and submicrometric dominant surfaces were allocated the value of 1.

Total porosity was determined on parallelepiped shaped samples of approximately 10 mm × 10 mm x 15 mm. The dimensions were measured with a precision caliper and the weight of the samples was measured with a precision scale. The porosity was derived from the theoretical density of a fully dense material with the crystalline phase composition determined by XRD.

To measure intragranular microporosity and macropore size,3 distinct back scattered images of the ground surfaces of the BGS were taken on 3 different sample of test materials and commercial articles. Randomly oriented lines were generated on the binarized images crossing a minimum of 100 pores on each image. The length of the line crossing each pore was measured owing to an image processing software (IMS, Imagic). The pore size was averaged for each image and for each sample. The ratio between the total length of the line and the sum of the lengths of the macropores was considered to be the intragranular macroporosity. Microporosity was derived from the subtraction of the total porosity and intragranular macroporosity.

To measure Tapped density, which represents the bulk density of granular material after controlled mechanical tapping, reflecting and intergranular porosity, a recipient of a volume of 1.4 cm^3 was filled with the different test materials and commercial articles. The mass of introduced material was measured owing to a scale after it was tapped in a controlled manner. The mass was then divided by the volume of the container to derive the tapped density. A total of 3 separate determinations were made and averaged for each BGS.

2.3. Mineralization ability tests

2.3.1. Simulated body fluid

An aqueous solution containing sodium, chloride, calcium and

Table 2
Host Reaction Scoring System for implantation sites adapted from ISO 10993-6:2016(E) (HPF = High Power Field).

CELL TYPE/RESPONSE	Score				
	0	1 (Minimal)	2 (Slight)	3 (Moderate)	4 (Marked/severe)
Polymorphonuclear cells	0	Rare,1-5/HPF	5-10/HPF	Heavy infiltrate	Packed
Lymphocytes	0	Rare,1-5/HPF	5-10/HPF	Heavy infiltrate	Packed
Plasma cells	0	Rare,1-5/HPF	5-10/HPF	Heavy infiltrate	Packed
Macrophages	0	Rare,1-5/HPF	5-10/HPF	Heavy infiltrate	Packed
Giant cells	0	Rare,1-2/HPF	3-5/HPF	Heavy infiltrate	Sheets
Necrosis	0	Minimal	Mild	Moderate	Severe
Neovascularization	0	Minimal capillary proliferation, focal, 1-3 buds	Groups of 4-7 capillaries with supporting fibroblastic structures	Broad band of capillaries with supporting structures	Extensive band if capillaries with supporting fibroblastic structures
Fibrosis/Fibroplasia	0	Narrow band	Moderately thick band	Thick band	Extensive band
Fatty infiltrate	0	Minimal	Mild	Moderate	Severe
Edema	0	Minimal	Mild	Moderate	Severe
Hemorrhage	0	Minimal	Mild	Moderate	Severe
Muscle fibers, degeneration/ regeneration	0	Minimal	Mild	Moderate	Severe

Table 3
Additional parameters evaluated during histopathology examination to assess osteoinductivity.

OSTEOINDUCTION	Score				
	0	1 (Minimal)	2 (Slight)	3 (Moderate)	4 (Marked/ Severe)
Ossification centers, early-stage (Mesenchymal)	None	Minimal	Mild	Moderate	Severe
Ossification centers, late-stage (Woven bone)	None	Minimal	Mild	Moderate	Severe
Cartilage	None	Minimal	Mild	Moderate	Severe
Bone marrow	None	Minimal	Mild	Moderate	Severe

phosphate ions was chosen as simulated body fluid (SBF) incubation solution as proposed in Ref. [41] and modified from [42]. A calcium rich solution (SBF-A) and a phosphate rich solution (SBF-B) were added in equal volume to produce the final SBF solution right before the assays (Table 1). CO_2 buffered simulated body fluid.

An aqueous solution containing sodium, chloride, calcium and phosphate and carbonate ions was chosen as CO_2 buffered simulated body fluid (BSBF) incubation solution as proposed in Ref. [43]. A calcium rich solution (BSBF-A) and a phosphate rich solution (BSBF-B) were added in equal volume to produce the final SBF solution right before the assays (Table 1).

Titrator units (Titrando 907, Metrohm) were used to measure pH with an internal reference pH electrode. Either a pH electode coupled with a temperature sensor (Unitrode, Metrohm) in case of low solid to liquid (Low S/L) assays, or a pH electrode with a small diameter capable of entering wells of a 48 well plate were used (Biotrode, Metrohm) for the high liquid to solid (high S/L) experiments. pH was monitored continuously in the low solid-to-liquid (S/L) experiment during 22h in triplicate. For each time point in the high S/L experiment (0.01 h, 2.25 h, 22 h), measurements were performed in quadruplicate. The 22 h monitoring period was selected to capture the initial rapid ion-exchange/acidification phase that dominates during the first day of SBF incubation, while providing a practical overnight window for continuous measurements; prior reports indicate that the largest changes typically occur within 24 h and approach quasi-equilibration within this timeframe.

Low S/L ratio tests were performed by adding 300 mg of BGS to 200 mL (1.5×10^{-3} g mL^{-1}) of SBF under constant propeller agitation. High S/L ratio experiments (0.2 g mL^{-1}) were performed in 3 different liquids, SBF (mineralization), modified BSBF (mineralization buffered) and ultrapure water (leachable test). 200 mg of material was weighed and placed in the well of a 48 well plate. The material was covered with 1 mL of incubation solution (SBF, modified BSBF, ultrapure water). The mineralization test in BSBF was performed in a CO_2 incubator set to maintain a 5% CO_2 atmosphere.

2.3.2. Total Ca and P quantification

Samples were taken from the low S/L and high S/L experiment at different time points with the method described in Ref. [25]. Triplicate samples were extracted for each time point for the low S/L experiments. Quadruplicate samples were extracted for each time point for the high S/L experiments. Samples were filtrated with nylon membrane filters of 0.2 μm (Rotilabo Nylon syringe filter, Carl Roth).

The solutions were analyzed using ICP-MS (Agilent 7700 ×, Agilent Technologies). To quantify the concentration of calcium and phosphate in the SBF incubated solution, the (solution) samples were diluted 1:100 in the same acid solution. The diluted samples were analyzed using ICP-MS (Agilent 7700 ×, Agilent Technologies). $_{23}$ (HNO_3Rotipuran Supra, Carl Roth), and 0.01 % HF (HF, Trace SELECT Ultra, Sigma Aldrich). The solutions were analyzed using ICP-MS (Agilent 7700 ×, Agilent Technologies). ^{44}Ca signals were calibrated against a certified single-element Ca standard (Karl Roth) and ^{31}P signals were calibrated against a multi-element standard solution (IV-ICPMS-71A, Inorganic Ventures). Calibration drifts were corrected according to the calcium standard measured after every 8 samples and according to a 20 ppb internal In/Sc/Bi standard solution (Inorganic Ventures) measured along with each sample. Finally, the mean values of three measurements per sample were determined.

2.4. Animal Study

The animal study was performed at a AAALAC International accredited facility (NAMSA, Northwood, OH, USA) that maintains an approved Animal Welfare Assurance on file with the National Institutes of Health, Office for Laboratory Animal Welfare. The study protocol was reviewed and approved by NAMSA's Institutional Animal Care and Use Committee (IACUC) prior to its execution.

Each test material was supplied as five separate packages of 3.79 – 3.87g of white granules packaged in double blisters, themselves packaged in a cardboard box sterilized at 25-37 KGy by X-Ray irradiation. The test materials and inside packaging containing the article were sterile and handled appropriately. Each lot was weighed to obtain eight portions of 120 ± 20 mg (0.120 ± 0.020 g) of article (one portion per implant site). Each portion was hydrated with sterile saline and loaded into sterile, 0.3 mL cut off tip syringes. Only the minimum amount of saline was used to hydrate each portion of test material. The sample was not over hydrated. All test material lots were implanted as prepared.

Before implantation, each mouse was weighed. On the day of surgery, each animal was injected subcutaneously with the analgesic

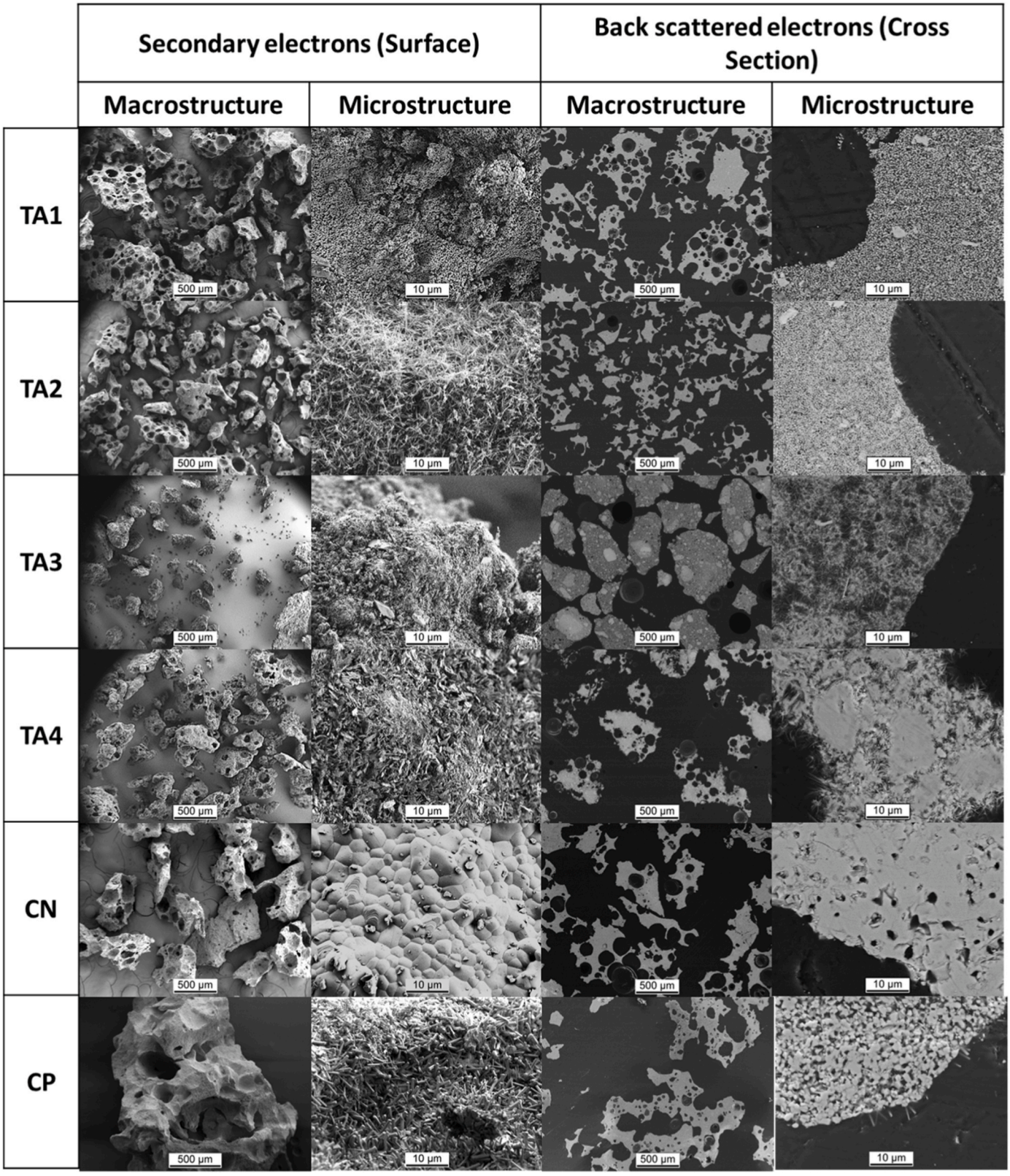

Fig. 1. Scanning electron micrographs of the surface and cross section of the granules allowing to observe, the size of the granules, surface microstructure and topography, and the presence of macroscopic and microscopic intragranular pores. Abbreviations: TA = non-commercial test material prototypes (labeled TA1–TA4); CN = cyclOs (Mathys Ltd); CP = MagnetOs (Kuros Biosciences); BGS = bone graft substitute; CaP = calcium phosphate.

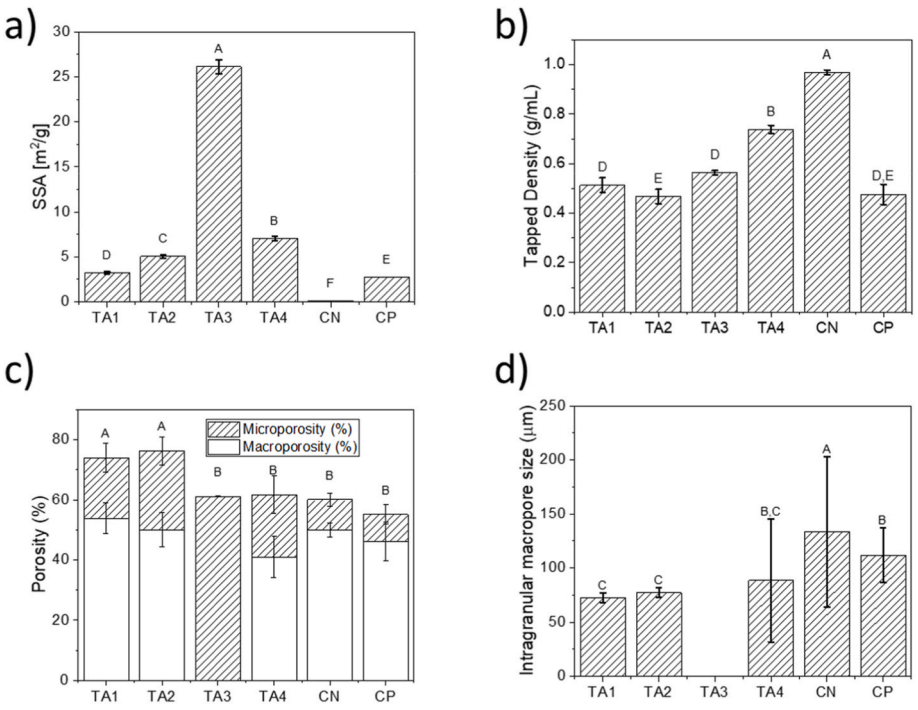

Fig. 2. Physical properties of the test materials and controls. a) specific surface area measured by nitrogen adsorption, b) Tapped density, c) Total, macro and microporosity as measured by dimensional measurements and image analysis, d) Intragranular macropore size measured by image analysis. Statistically significant differences are presented by grouping letters. Groups statistically equivalent (Tukey's post hoc test $p > 0.01$) show the same letter. Groups statistically different ($p < 0.01$) present different letters. Abbreviations: TA = non-commercial test material prototypes (labeled TA1–TA4); CN = cyclOs (Mathys Ltd); CP = MagnetOs (Kuros Biosciences); BGS = bone graft substitute; CaP = calcium phosphate.

buprenorphine at a dose of 0.5 mg/kg prior to surgery. The animals were placed under anesthesia with isoflurane via anesthetic induction chamber and anesthetic mask, as needed. A veterinary ophthalmic ointment was applied to both eyes of each animal to protect the corneas from drying. Once the anesthetic had taken effect, the posterior and lateral sides of both hind limbs were clipped free of fur, as necessary. The implant area was scrubbed with a germicidal soap, wiped with 70% alcohol and the skin painted with an antiseptic such as povidone iodine. After completion of the surgical prep, the animals were positioned in the surgical field in lateral recumbency, draped in a routine fashion and anesthesia was maintained via the anesthetic mask.Using aseptic surgical techniques, a skin incision approximately 1 cm long was made over the posterior lateral aspect of the right upper hind limb, parallel to the femur. Using blunt dissection, a pocket was created between the superficial gluteal muscle and bicep femoris muscle. The appropriate article was placed in the pocket (see Supplementary Table 1). The muscle fascia over the implant was closed with a non-absorbable 6-0 Prolene suture and the skin was closed with tissue glue. The left leg was similarly implanted. The remaining animals were similarly operated, receiving the appropriate material per Supplementary Table 1. The day of implantation was considered day 0. Care was taken so that the implant did not touch a bone as this could have biased the data. An intermuscular implantation was performed to minimize the amount of blood in the implant site to allow for a more accurate assessment of the osteoinduction of the product. Any excessive bleeding observed was documented.

At 35 days and 56 days after implantation, the designated animals were euthanized by carbon dioxide inhalation. The entire limb (from both sides, left and right) was removed and the skin was dissected free (extraneous muscles were not dissected free). The sites were placed in a labeled cassette and/or container containing 10% neutral buffered formalin (NBF) for fixation.

After fixation, all implant-bearing tissues were excised, bisected, and then decalcified in a commercial solution. Decalcification was carefully controlled to maintain sufficient tissue rigidity for sectioning. Decalcified specimens were processed for paraffin embedding and oriented with cut faces down, one block per explant. From each block, one slide from the first complete section was prepared, and two additional step sections were cut at ~200-µm intervals; section thickness was 4–6 µm. This yielded six sections per bisect (12 per site). For each bisect, three sections were stained with hematoxylin–eosin (H&E) and three with Masson–Goldner Trichrome (MGT). Slides were imaged and then submitted to the pathologist for evaluation.

Slide readings were performed on digital slides (WSI) in the bioimage analysis software QuPath, version 0.3.2. The microscopic findings were recorded during histopathology examination by a certified pathologist (co-author of the present study, R. De Miguel) and directly entered in an MS EXCEL file. A semi-quantitative histopathology evaluation was performed per section using the HE and MGT according to an adapted and extended ISO 10993-6:2016 scoring system (Tables 2 and 3). Scoring data was initially summarized first per implant site and further per group condition.

Quantitative evaluation was made in Aperioscope, quantitative pathology and bioimage analysis software. On the HE-stained digital slides (WSI) for all articles the overall area of interest (AOI), excluding surrounding muscle fibers, were manually annotated. Each Identified bone spicule within the area was manually drawn. The number (N), perimeter (P_A) and area (S_A) of all drawn bone spicule and area of interest were obtained.

Bone area (BA) over total area (TA) was determined as follows:

$$BA \Big/ TA = \frac{\sum_{1}^{N} S_A}{AOI}$$

Spicule density (Sp.D.) was calculated as follows:

$$S.D. = \frac{N}{AOI}$$

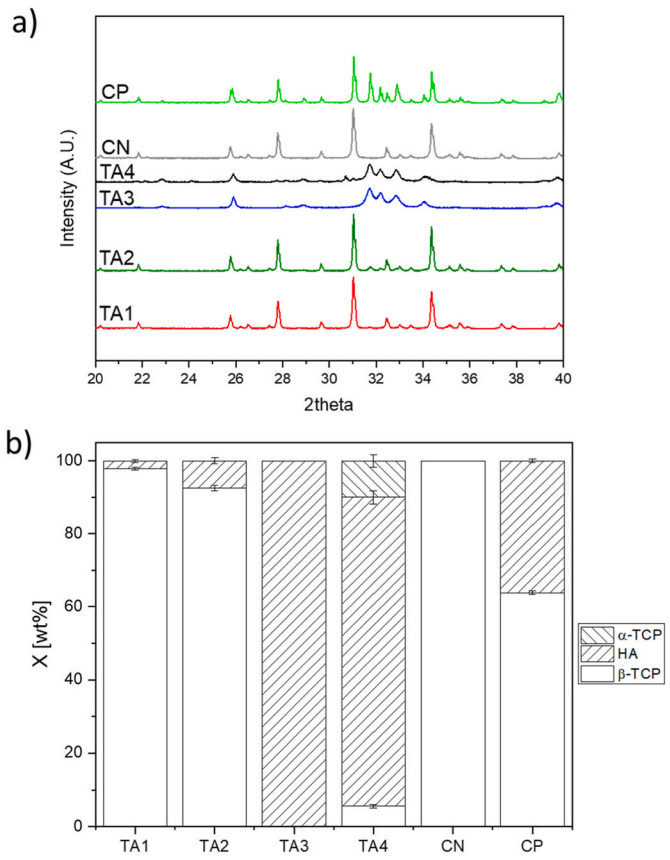

Fig. 3. X-ray powder diffraction results of the test materialtest materials and controls. a) Normalized X-ray diffraction patterns, b) Phase quantification resulting from the rietveldt refinement of the patterns with Profex 2.0. Abbreviations: TA = non-commercial test material prototypes (labeled TA1–TA4); CN = cyclOs (Mathys Ltd); CP = MagnetOs (Kuros Biosciences); BGS = bone graft substitute; CaP = calcium phosphate.

2.5. Statistical Analysis

ANOVA was performed with dedicated software (Minitab), Tukey post hoc test was applied on individual means. Statistical significance was considered when $p < 0.01$. ANOVA was executed separately for each postimplantation time and differences are presented by grouping letters. Means that share the same letter belong to the same statistical group and are not significantly different whereas means with no letters in common differ significantly according to the selected significance level.Spearman's rank correlation was employed to assess the relationships between MIHO-selected outcomes and a set of physical predictors (tapped density, intergranular porosity, SSA, topography, macropore size, microporosity, total porosity) as well as chemical predictors, including phase-composition variables (β-TCP, HA, and α-TCP contents) and solution-change metrics (ΔpH, ΔCa, ΔPO_4, Ca/P), determined for four solution tests (low S/L SBF, high S/L in H_2O, SBF, and BSBF). To capture bone early stage formation ESOC pathological scores were used, bone area over total area of interest (BA/TA), bone spicule number over total area of interest (Spicule density) and early inflammation resolution (polymorphonuclear cells) employing Spearman's ρ and associated p values for significance. Spearman's ρ captures monotonicity and is insensitive to scale and mild outliers, which makes it a tool of choice for this type of heterogenous correlation.

3. Results

3.1. Physico-chemical characterizations

Non-commercial test materials (TA1–TA4; 'TA') were compared with the commercial references cyclOs (CN) and MagnetOs (CP). All test materials consisted of irregular granules (Fig. 1). Except for CP (1-2 mm), all granules had a size between 0.125- and 0.7-mm. Field-emission SEM revealed submicron surface features on all materials except CN. Back-scattered imaging showed numerous concave intragranular macropores in TA1, TA2, TA4, CN, and CP, and comparatively fewer in TA3 (Fig. 1). Specific surface area (SSA) ranged from approximately 3 to 26 $m^2\ g^{-1}$ across the prototypes, all exceeding the values of CN and CP (Fig. 2a). Tapped density (reflecting packing efficiency and intergranular porosity) was highest for CN (0.97 g mL^{-1}) and lowest for CP and TA2 (0.47 g mL^{-1}) (Fig. 2b). Total porosity varied from about 55% (CP) to 76% (TA1) (Fig. 2c). Mean intragranular macropore size were below 100 μm for all prototypes and larger for the commercial references (Fig. 2d). Collectively, these findings indicate that the prototypes integrate submicron surface texture with curvature-rich porosity—two structural attributes subsequently linked to enhanced bone formation.

X-ray diffraction identified single-phase HA in TA3 and single-phase β-TCP in CN. TA1, TA2, and CP were biphasic (HA + β-TCP), with CP exhibiting the highest HA fraction, whereas TA4 was triphasic (HA > β-TCP > α-TCP). Broadened diffraction peaks indicated lower crystallinity in TA3 and TA4 (Fig. 3).

3.2. Solution Reactivity Under High Solid-To-Liquid (High S/L) Conditions

Ion exchange (calcium, phosphate, Ca/P ratio) and pH evolution were monitored in ultrapure water, simulated body fluid (SBF), and CO_2/HCO_3^--buffered SBF (BSBF). In ultrapure water, TA3 and TA4 induced the greatest phosphate release and most pronounced acidification, with pH decreases of approximately 1.5–2 units (Fig. 4). TA1, TA2 and CN produced alkaline, calcium-rich eluates, whereas CP showed intermediate values. Ca/P ratios were below 1 for CP, TA3, and TA4, but markedly higher for TA1 and TA2 (Fig. 4; Fig. S1). In SBF, TA3 and TA4 increased calcium and phosphate concentrations accompanied by pH decrease, whereas TA1 and TA2 depleted phosphate (Fig. 5). CP displayed intermediate behavior and CN produced minimal changes. The resulting solution Ca/P approached unity for TA3 and TA4 and remained much higher for TA1 and TA2 (Fig. 5; Fig. S2). Comparable experiments conducted at low S/L ratio yielded qualitatively similar but less pronounced trends, confirming that the observed ion-exchange behavior is intrinsic to material composition rather than an artifact of testing concentration (Fig. S3). In buffered SBF (BSBF, Table 1), pH shifts were attenuated by buffering, yet TA3 and TA4 continued to cause the strongest acidification and phosphate elevation. Under these more physiologically relevant conditions, Ca/P again fell below ~0.5–1 for TA3, TA4, and CP, while remaining high for TA1 (Fig. 6). Across all media, TA3 and TA4 consistently promoted phosphate release and acidification, TA1 and TA2 induced the opposite trend, and CP and CN showed intermediate responses. None of the BGS experienced crystalline phase changes upon incubation in any of the liquids.

3.3. Ectopic Bone Formation In Vivo (FVB Mice Intramuscular Model)

At 35 days, no bone formation was observed in CN, CP, TA1, or TA3. TA2 exhibited occasional bone nodules (2/4 implants, 7/24 sections), and TA4 showed rare nodules (2/24 sections) (Table 3). At 56 days, CN, CP, and TA1 remained negative, TA2 and TA3 displayed sporadic bone formation (2/24 and 4/24 sections, respectively), whereas TA4 exhibited consistent bone formation in 21/24 sections across all implants (Figs. 7 and 8; Fig. S4–5; Table 3). TA2 presented less bone across slides

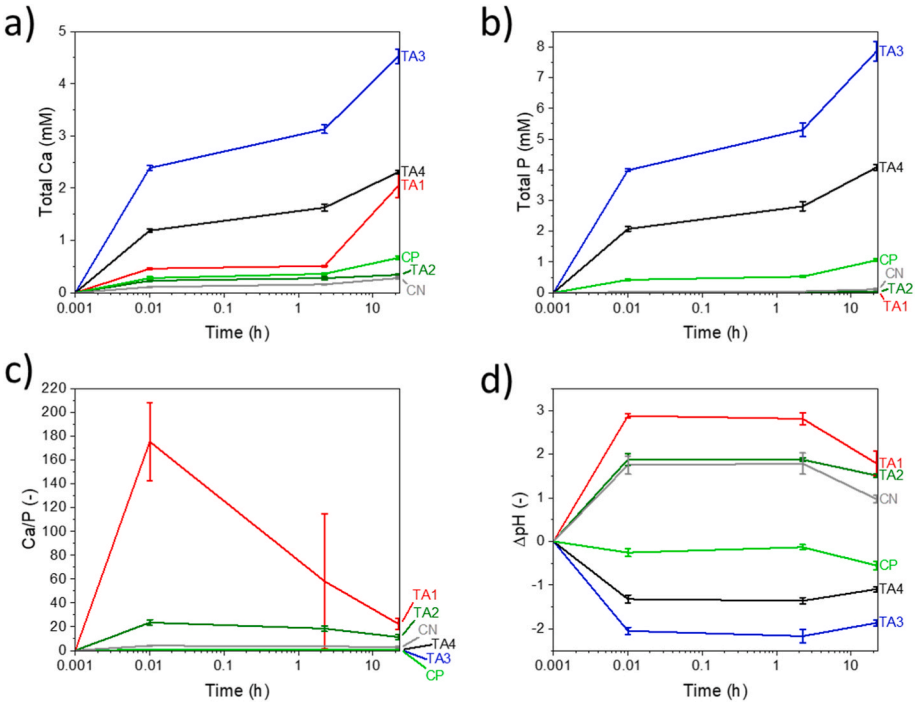

Fig. 4. High solid to liquid test in ultrapure water test results in ultrapure water for the test materials. a) Evolution of the Calcium concentration, b) Evolution of the Phosphate concentration c) Evolution of the Calcium to phosphorus concentrations ratio. d) pH decrease during the leachable test. Abbreviations: TA = non-commercial test material prototypes (labeled TA1–TA4); CN = cyclOs (Mathys Ltd); CP = MagnetOs (Kuros Biosciences); BGS = bone graft substitute; CaP = calcium phosphate.

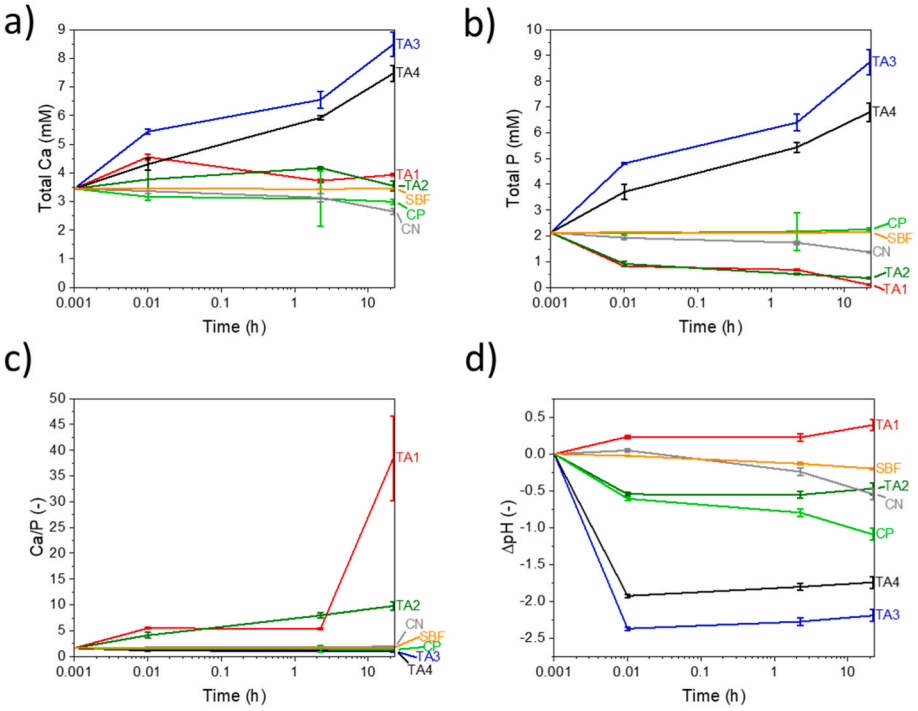

Fig. 5. High solid to liquid test in SBF results for the test materials and control in high solid to liquid conditions a) Calcium concentration, b) Phosphate concentration c) Calcium to Phosphate concentrations ratio. d) pH drop curves, after 22h of mineralization test. Abbreviations: TA = non-commercial test material prototypes (labeled TA1–TA4); CN = cyclOs (Mathys Ltd); CP = MagnetOs (Kuros Biosciences); BGS = bone graft substitute; CaP = calcium phosphate.

and implants at 56 days than at 35 days postimplantation, possibly due to animal variability. Histomorphometric and semiquantitative pathology analyses corroborated these observations, with TA4 showing the highest bone area fraction and spicule density at 56 days (ANOVA/Tukey, $p < 0.01$) (Fig. 9c and d). Early ossification centers were most prominent in TA4 at 35 days and remained elevated at 56 days. Late ossification (woven bone) appeared in TA2 and TA4 at 35 days and predominated in TA4 at 56 days (Fig. 9).

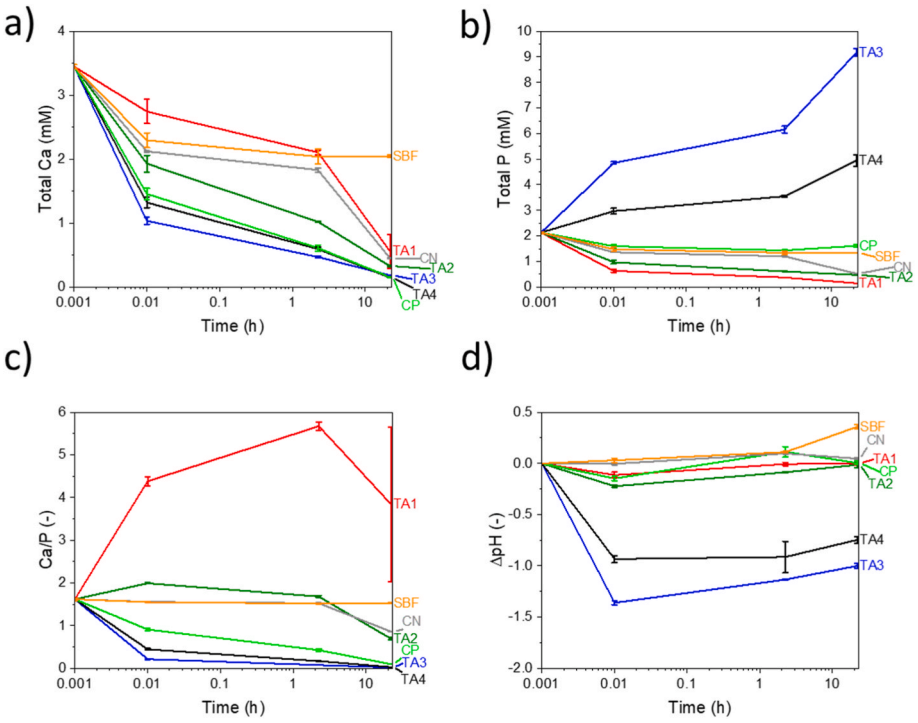

Fig. 6. – Results of the high solid to liquid test in CO_2 buffered simulated body fluid (BSBF) for the test materials a) Calcium concentration, b) Phosphate concentration c) Calcium to phosphate concentrations ratio. d) pH decrease evolution during the mineralization test in BSBF. Abbreviations: TA = non-commercial test material prototypes (labeled TA1–TA4); CN = cyclOs (Mathys Ltd); CP = MagnetOs (Kuros Biosciences); BGS = bone graft substitute; CaP = calcium phosphate.

3.4. Host Tissue Reaction

To facilitate interpretation of the histopathology, the inflammatory infiltrate was scored by separating the major immune cell populations recommended in the ISO 10993-6–adapted scheme (see Table 5, as these populations reflect distinct phases of the host response to implanted biomaterials. Polymorphonuclear cells (PMNs) were assessed as indicators of an acute inflammatory component, whereas macrophages and multinucleated giant cells were evaluated to capture the macrophage-driven foreign body reaction typically observed around particulate implants. Lymphocytes (and plasma cells) were included to identify a potential chronic/adaptive immune component. Therefore, the correlation analysis focused on the subset of cell types that exhibited clear and statistically meaningful differences between materials, while parameters with uniformly low and statistically equivalent scores (e.g., lymphocytes/plasma cells) were not emphasized to avoid over-interpretation. Macrophage infiltration was moderate in all groups at both time points (Table 4, Fig. 10). Lymphocyte density tended to be higher in CN, CP, TA1, and TA2 and lower in TA3 and TA4. Polymorphonuclear cells were more pronounced in CN, CP, TA1, and TA3 at 35 days and least evident in TA4 at 56 days. Giant cells surrounded most granules, while plasma cells were scarce. Neovascularization increased by 56 days, with the strongest response in TA3. The fibrous capsule was dense at 35 days and thinned for CN and TA2 by 56 days. No cartilage or marrow islands were detected (Table 4; Fig. S6). Representative histology of TA4 illustrates the transition from early ossification centers at 35 days to woven bone at 56 days within and around concave pores (Fig. 11).

3.5. Correlation analysis: physical structure and interfacial chemistry jointly predict material induced heterotopic ossification

Spearman correlation analysis (Fig. 12) revealed three principal predictive axes linking material properties to in-vivo outcomes. Larger concave intragranular macropores (Materials presenting intragranular macropores with a greater characteristic size as quantified by the size distribution in Fig. 2d) favored initiation, correlating positively with the number of early ossification centers at 35 and 56 days ($\rho \approx 0.56$–0.58; $p \leq 0.016$). Submicron surface texture favored consolidation, as SSA and microporosity correlated strongly with spicule density and bone area at 56 days (SSA vs. spicule density: $\rho = 0.804$, $p = 5.8 \times 10^{-5}$; SSA vs. bone area: $\rho = 0.688$, $p = 0.0016$). Phosphate-rich and mildly acidic conditions under confinement further promoted bone formation, with greater phosphate release and lower pH correlating with higher spicule density and bone area (ΔpH in buffered SBF vs. spicule density: $\rho = -0.726$, $p = 6.4 \times 10^{-4}$; ΔpH vs. bone area: $\rho = -0.694$, $p = 0.001$). Interestingly phosphate net change correlated with net pH change (Fig. S7). Conversely, a higher Ca/P release ratio correlated negatively with spicule density across media. Phase composition largely reflected the interfacial milieu created by each phase: α-TCP content correlated positively with early and late bone formation, HA content correlated positively with late outcomes, and β-TCP content correlated negatively with late outcomes. Material-level analyses using per-material medians preserved these associations, underscoring their robustness (Fig. 12).

3.6. Integrative interpretation

Materials combining curvature-rich intragranular pores, with submicron texture (Fig. 1) and specific interfacial chemistry (releasing acidic phosphate species, Figs. 4–6) generated confined microenvironments that were phosphate-rich and mildly acidic—conditions that most strongly predicted late ectopic bone formation (Figs. 8 and 9). Among all prototypes, TA4 expressed this combined signature most distinctly and achieved the highest and most consistent bone formation at 56 days. Practically, ΔpH, ΔPO_4, and Ca/P measured under high S/L conditions, together with pore curvature and submicron texture, constitute concise and predictive indicators of ectopic bone formation in this model (Figs. 4–6, 12).

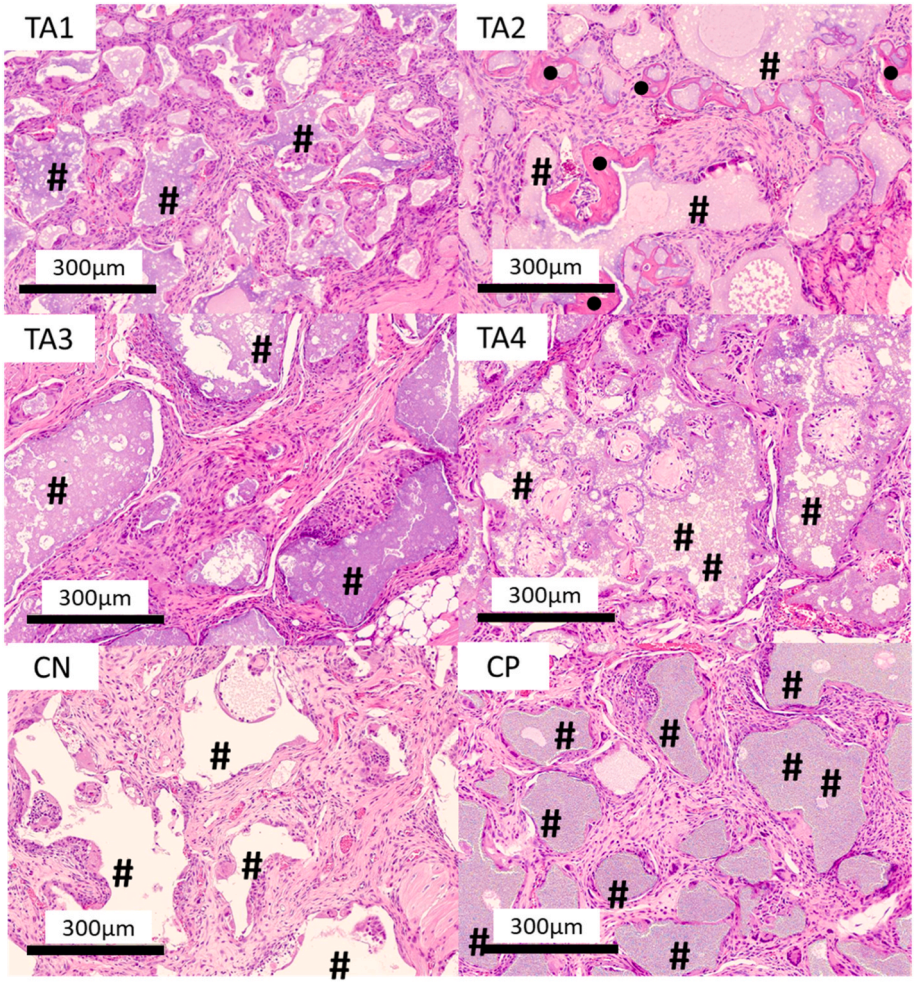

Fig. 7. Optical transmission images of the histological slices of muscle tissue containing the test materialtest material and controls after their explantation 35d postimplantation. Tissues were stained with hematoxilin and eosin. Bone(●), CaP BGS (#).Abbreviations: TA = non-commercial test material prototypes (labeled TA1–TA4); CN = cyclOs (Mathys Ltd); CP = MagnetOs (Kuros Biosciences); BGS = bone graft substitute; CaP = calcium phosphate.

4. Discussion

Through four decades of work, researchers have designated a set of physicochemical features that are suspected to be associated with MIHO [44].

Physical features often cited as associated with MIHO comprise Specific Surface Area (SSA), porosity shape, size and architecture, microstructure and topography [45–50]. High specific surface area is generally regarded as positively correlated with MIHO outcomes. Barba et al. have shown that CDHA foams with specific surface area one order of magnitude higher than their BCP and β-TCP counterparts, elicit more consistent, earlier MIHO in a dog paravertebral implantation model [45]. Yuan et al. have shown that β-TCP porous granules and blocks with different SSA and otherwise similar crystalline phase composition elicit opposite MIHO response in canine and murine models of ectopic implantation [47,51–53]. Microporosity and topography/roughness, typically varied in calcium phosphate ceramics via sintering process parameter changes, are essentially covariant surrogates of SSA. Authors have pointed toward these features, without being able to deconvolute their individual contribution to MIHO but microstructural features (both micropores and surface crystals) in the submicron range seem to make consensus as essential feature for MIHO [21,44,48,54,55]. Another physical aspect that has drawn copious interest from researchers is the relationship between the pore size and architecture of CaP BGS and their MIHO capacity. Barba and Shi have demonstrated that even though a network of interconnected macroporosity is necessary it is not sufficient for MIHO [45,56]. Surface curvature matters and concave macropores have been identified as an essential structural characteristic of osteoinductive CaP-BGS [57]. It is worth noting that all of these physical features have chemical consequences by impacting surface chemistry and matter transport within the bone graft substitute [46,58,59].

On the chemical side, crystalline phase composition, solubility in water, calcium release, calcium to phosphorus releasing ratio and mineralization capacity in SBF type assays have all been identified as potential correlates of MIHO outcomes [44,54,60–62]. CaP crystalline phase MIHO potential is not a clear cut, CaP that have been studied are predominantly composed of 2 main phases: HA (sometimes calcium deficient, CDHA), and β-TCP or a mix thereof. Bohner and Miron have concluded that the MIHO potential of the phases was HA > BCP>β-TCP [23], while others have it in a different order β-TCP ~ BCP > HA [62–64]. The solubility of crystalline phases in water is frequently reported as impacting MIHO, despite being thermodynamically implausible because these phases are insoluble under physiological conditions. If solubility were relevant, it would pertain to other phases that are indeed soluble under this set of circumstances. Calcium-deficient hydroxyapatite (CDHA), often associated with MIHO, exhibits pronounced ion reactivity manifested by a decrease in calcium and pH, and an increase phosphate in surrounding media [29,65]. Its solubility is a controversial topic and these chemical changes are often attributed to the so-called hydrated layer [66–68], which chemical nature and behavior remains to be fully elucidated. Overall, how local pH shifts influence osteogenesis remains unresolved and appears strongly context

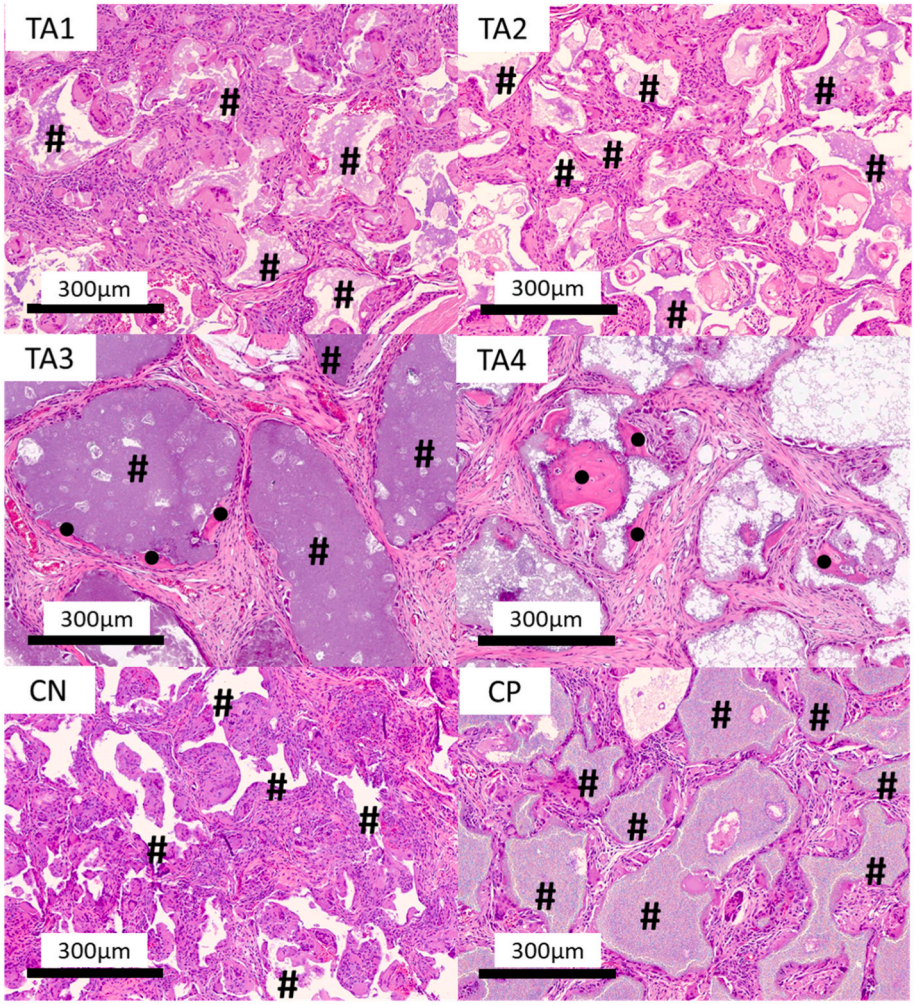

Fig. 8. Optical transmission images of the histological slices of muscle tissue containing the test material and controls after their explantation 56d postimplantation. Tissues were stained with hematoxilin and eosin. Bone(●), CaP BGS (#). Abbreviations: TA = non-commercial test material prototypes (labeled TA1–TA4); CN = cyclOs (Mathys Ltd); CP = MagnetOs (Kuros Biosciences); BGS = bone graft substitute; CaP = calcium phosphate.

dependent. Several controlled in vitro studies report that a mild alkaline extracellular pH supports osteoblast differentiation and matrix mineralization, with acidification suppressing ALP activity and mineralized nodule formation [69]. Conversely, other in vitro work in CaP conditioned environments has suggested that transient acidification coupled to phosphate release can promote MSCs commitment toward an osteoblastic lineage (e.g., increased ALP activity and osteogenic gene expression), consistent with the idea that ion-exchange signatures, not pH alone, may shape osteogenic signaling [28,29,70]. The Ca/P release ratio at the implant interface has been proposed as an informative proxy. One study observed that ratios of ~1.5–2.0 tracked with stronger osteoinductivity under comparable architectures, whereas lower ratios supported only osteoconduction [71]. Yet, Maazouz et al. reported an opposite trend, with higher Ca/P ratios inversely correlated with MIHO [25].

Despite this maturing picture, relatively few studies have explicitly decoupled chemistry from architecture/topography in models directly relevant to MIHO; most datasets vary multiple parameters at once, complicating attribution of causality to either set of factors [44,72,73]. Where attempts have been made (e.g., isolating surface microstructure from composition in controlled β-TCP/BCP systems or comparing otherwise matched scaffolds with altered pore geometry) results reinforce that both the chemical driving forces (ion-release balance, hydrolysis/reprecipitation pathways) and the physical field (curvature-rich, submicron-textured pores) are necessary co-determinants of osteoinduction [45,48,49,57]. Motivated by this gap, the present work set out to correlate MIHO outcomes quantitatively with both physical predictors (pore architecture, micro-/nano-texture, SSA, porosity) and chemical predictors (crystalline phase composition, Ca/P release ratio, ion reactivity, pH) within a harmonized framework, to clarify when and how each set of factors dominates, and how their coupling yields the osteoinductive niche.

To that aim Spearman correlations were used to quantify correlative monotonicity (ρ) and associated probabilities of false identification (p values), in this discussion values of $|\rho| > 0.5$ associated with $p < 0.05$ were considered. Spearman correlations of physical predictors (Tapped density, Intergranular porosity, SSA, Topography, Macropore size, Microporosity, Total porosity; Figs. 1 and 2) and chemical predictors (β-TCP content, HA content, α-TCP content (Fig. 3), ΔpH, ΔCa, ΔPO_4, Ca/P; for 4 different solution tests namely Low S/L SBF test, High S/L in H_2O, SBF, and BSBF (Figs. 4–6)) with MIHO selected outcomes instruct on the relationship between the microenvironment generated by the BGS and the biological reaction leading to bone formation (Fig. 12). On the physical side, the clearest early signal is the positive association between the presence/size of intragranular macropores and mesenchymal condensation loci: macropores correlate with ESOC (Fig. 9)at 35 days ($\rho = 0.583$, $p = 0.011$) and again at 56 days ($\rho = 0.557$, $p = 0.016$), indicating that the presence of more numerous concave cavities within granules favor the appearance of early ossification centers. By contrast, open porosity in bulk is not uniformly beneficial: total porosity is

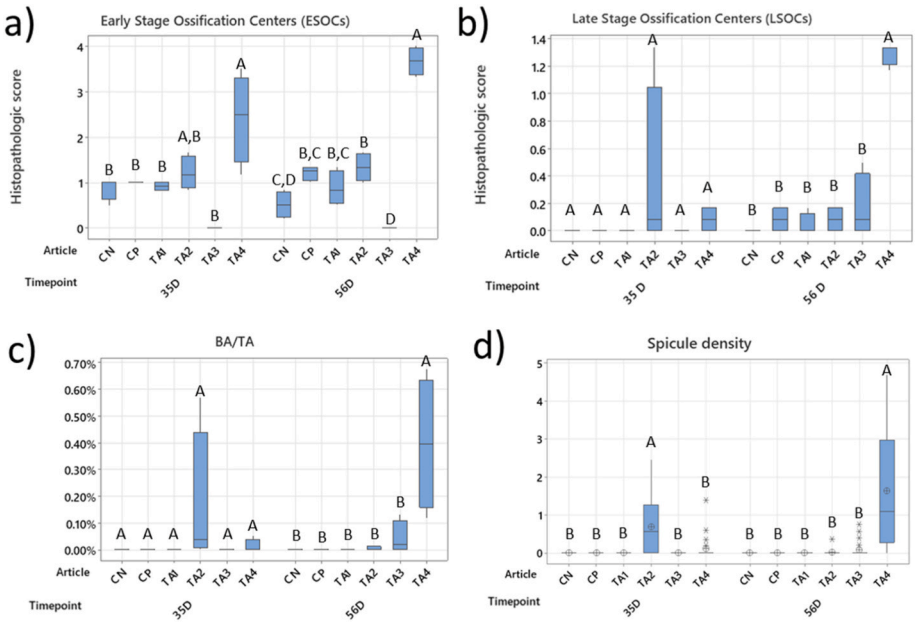

Fig. 9. Results of the histopathological evaluation of the histologies at 35 and 56 days postimplantation. a) Early stage ossification centers (ESOC), b) Late stage ossification centers (LSOC). c) Histomorphometric results of the bone area over total area (BA/TA) at both postimplantation time points. d) Spicule density (S.D., mm^{-2}). ANOVA was executed separately for each postimplantation time point. Statistically significant differences are presented by grouping letters. Groups statistically equivalent (Tukey's post hoc test $p > 0.01$) show the same letter. Groups statistically different ($p < 0.01$) present different letters. Abbreviations: TA = non-commercial test material prototypes (labeled TA1–TA4); CN = cyclOs (Mathys Ltd); CP = MagnetOs (Kuros Biosciences); BGS = bone graft substitute; CaP = calcium phosphate.

Table 4
– Bone occurrence distribution across animals, implantation sites and histological cuts. A) After 35 days postimplantation, B) After 56 days postimplantation. Abbreviations: TA = non-commercial test material prototypes (labeled TA1–TA4); CN = cyclOs (Mathys Ltd); CP = MagnetOs (Kuros Biosciences); BGS = bone graft substitute; CaP = calcium phosphate.

A).					
BGS	35d				Total
	Animal 1		Animal 2		
	left	right	left	right	
CN	0/6	0/6	0/6	0/6	0/24
CP	0/6	0/6	0/6	0/6	0/24
TA1	0/6	0/6	0/6	0/6	0/24
TA2	0/6	6/6	1/6	0/6	7/24
TA3	0/6	0/6	0/6	0/6	0/24
TA4	0/6	1/6	0/6	1/6	2/24
B).					
BGS	56d				Total
	Animal 3		Animal 4		
	left	right	left	right	
CN	0/6	0/6	0/6	0/6	0/24
CP	0/6	0/6	0/6	0/6	0/24
TA1	0/6	0/6	0/6	0/6	0/24
TA2	1/6	1/6	0/6	0/6	2/24
TA3	1/6	3/6	0/6	0/6	4/24
TA4	6/6	5/6	5/6	5/6	21/24

positively related to spicule density at 35 days ($\rho = 0.523$, $p = 0.026$), but macroporosity (the volumetric fraction of macro-voids) is negatively related to spicule density at 56 days ($\rho = -0.475$, $p = 0.046$). This inversion is consistent with the idea that a certain amount of confinement and curvature is required for bone to sprout: too high of a macroporosity may shorten residence times and dissipate the sustained local ionic homeostatic imbalance that concavities generate [23,26]. Importantly, microstructural measures that proxy submicron texture and reactive area become dominant in late endpoints: specific surface area (SSA) is very strongly and positively associated with spicule density at 56 days ($\rho = 0.804$, $p = 5.8 \times 10^{-5}$) and with BA/TA at 56 days ($\rho = 0.688$, $p = 0.0016$); microporosity shows the same pattern (spicule density 56 days: $\rho = 0.655$, $p = 0.0032$; BA/TA 56 days: $\rho = 0.559$, $p = 0.0159$). Together with the macropore results, this argues for a hierarchy of physical control: macropores (concavities) serve as the terrain for bone sprouting, while micro/nano-textured surfaces inside those concavities (captured by SSA and microporosity) become the influential factors of later bone growth (spicules and BA/TA) at 56 days. A direct comparison of TA3 and TA4 illustrates that MIHO in this panel cannot be predicted from SSA or phase composition alone: although TA3 exhibits a higher SSA and no detectable α-/β-TCP in our XRD quantification (reported as 0%), it lacks intragranular macroporosity. By contrast, TA4 couples curvature-rich intragranular macropores with submicron texture while its HA content is lower (~82–87%), but presented superior in vivo outcome.

The chemical surrogates show a complementary instructive signature. Nearly every metric that encodes an acidifying, phosphate-enriching microenvironment relates positively to the late ectopic readouts. At high solid-to-liquid (S/L) ratios, which best mimic the confined fluid in pores, greater phosphate liberation is associated with more bone: ΔPO_4 (high S/L, SBF) vs spicule density 56 days has $\rho = 0.524$ ($p = 0.025$); ΔPO_4 (high S/L, H_2O) vs spicule density 56 days is even stronger ($\rho = 0.666$, $p = 0.0025$). In the same high S/L setting, acidification (more negative ΔpH) correlates with better outcomes: ΔpH (high S/L, SBF) vs spicule density 56 days $\rho = -0.563$ ($p = 0.015$); the buffered High S/L BSBF reproduces this trend with larger magnitude (ΔpH high S/L, BSBF vs spicule density 56 days; $\rho = -0.726$, $p = 6.4 \times 10^{-4}$) and the same ΔpH marker is also negatively associated with BA/TA at 56 days ($\rho = -0.694$, $p = 0.001$). ΔCa High S/L SBF positively correlates with spicule density 56 days ($\rho = 0.671$, $p = 0.0023$), But this trend disappears in the buffered BSBF assay, suggesting that Ca release is unlikely to occur in vivo. However, whenever the release balance is expressed as a Ca/P ratio, the association is negative, Ca/P (high S/L,

Table 5
– Summarized results of the histopathological assessment for the host reaction and the evaluated at both 35 and 56 days for all commercial and test BGS. Abbreviations: TA = non-commercial test material prototypes (labeled TA1–TA4); CN = cyclOs (Mathys Ltd); CP = MagnetOs (Kuros Biosciences); BGS = bone graft substitute; CaP = calcium phosphate.

Timepoint		35 DAYS						56 DAYS					
BGS		CN	CP	TA1	TA2	TA3	TA4	CN	CP	TA1	TA2	TA3	TA4
Host reaction	Polymorphonuclear cells	1.0	1.6	1.6	1.0	0.9	0.3	1.0	2.7	2.0	1.3	1.0	0.3
	Lymphocytes	2.5	2.9	2.8	2.8	2.0	2.1	2.7	2.5	2.6	2.7	2.0	2.0
	Plasma cells	1.0	1.0	1.5	1.3	1.0	1.0	1.0	1.0	1.3	1.0	1.0	1.0
	Macrophages	2.6	2.9	2.6	2.5	2.7	2.2	2.7	2.7	2.5	2.6	2.6	2.0
	Giant cells	2.0	2.4	2.4	2.2	1.5	2.0	2.3	2.3	2.3	2.8	1.9	2.2
	Necrosis	0.0	0.0	0.0	0.0	0.0	0.0	0.0	0.0	0.0	0.0	0.0	0.0
	Neovascularization	2.0	2.0	1.5	1.8	2.0	2.0	2.0	2.0	1.5	2.0	2.3	2.0
	Fibroplasia/Fibrosis	3.0	2.7	2.8	2.9	3.0	3.0	2.4	3.0	3.0	2.3	3.0	3.0
	Fatty, Infiltrate	1.1	2.2	1.0	1.5	1.0	1.1	1.7	1.5	1.1	1.1	1.6	1.6
	Edema	0.0	0.0	0.0	0.0	0.0	0.0	0.0	0.0	0.0	0.0	0.1	0.0
	Hemorrhage	0.8	0.7	0.6	1.0	0.3	0.3	0.4	0.3	1.0	0.0	0.0	0.0
	Muscle fibers, degeneration/regeneration	2.0	2.0	2.0	2.0	2.0	2.0	2.0	2.0	2.0	2.0	2.0	2.0
	Cartilage	0.0	0.0	0.0	0.0	0.0	0.0	0.0	0.0	0.0	0.0	0.0	0.0
	Bone marrow	0.0	0.0	0.0	0.0	0.0	0.0	0.0	0.0	0.0	0.0	0.0	0.0

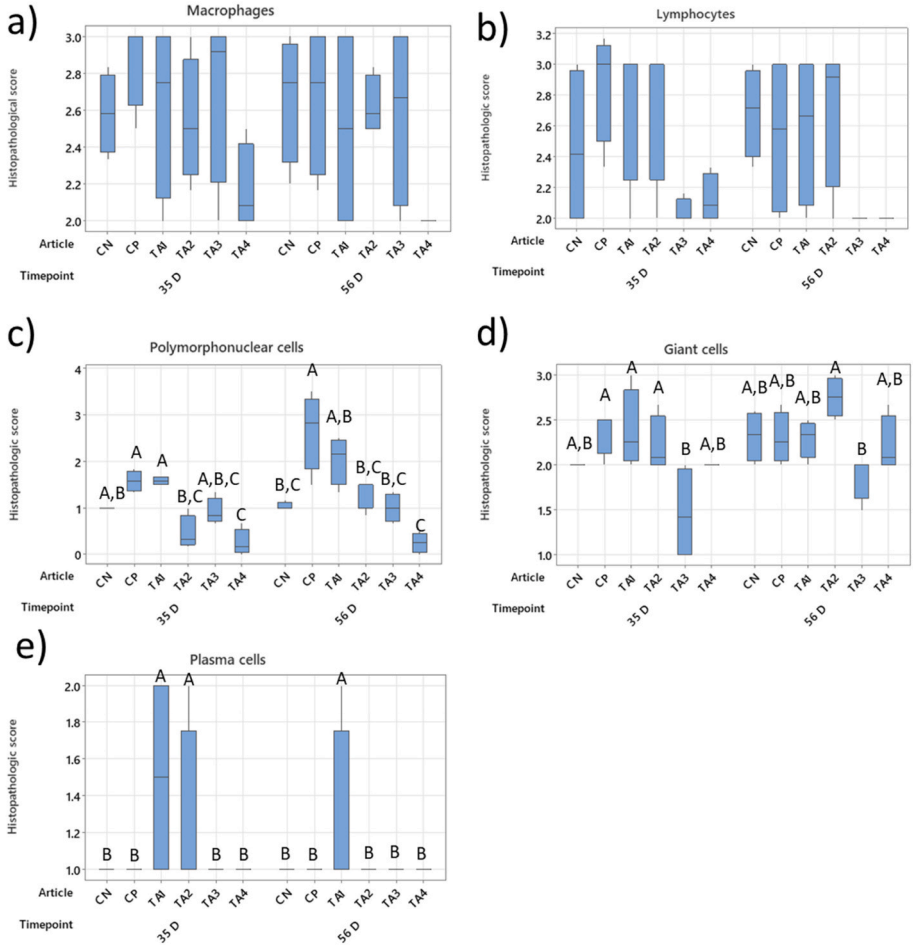

Fig. 10. Results of the histopathological evaluation of the histologies at 35 and 56 days postimplantation. a) Macrophages histopathologic scores, b) Lymphocytes histopathologic scores, c) polymorphonuclear cells histopathologic scores, d) Giant cells histopathologic scores. e) Plasma cells histopathologic scores. ANOVA was executed separately for each postimplantation time point. Statistically significant differences are presented by grouping letters. Groups statistically equivalent (Tukey's post hoc test $p > 0.01$) show the same letter. Groups statistically different ($p < 0.01$) present different letters. No letters are displayed in the absence of statistically significant differences. Abbreviations: TA = non-commercial test material prototypes (labeled TA1–TA4); CN = cyclOs (Mathys Ltd); CP = MagnetOs (Kuros Biosciences); BGS = bone graft substitute; CaP = calcium phosphate.

BSBF) vs spicules 56 days $\rho = -0.667$ ($p = 0.0025$); Ca/P (high S/L, H_2O) vs spicules 56 days $\rho = -0.544$ ($p = 0.0197$); Ca/P (high S/L, SBF) vs spicules 56 days $\rho = -0.483$ ($p = 0.042$). Read together, these three axes (↑ΔPO_4, ↓ΔpH, ↓Ca/P) all point to the same niche: a phosphate-rich, mildly acidic, interfacially controlled hydrolysis environment in the confined liquid of curvature-rich pores (Fig. S7). The fact that analogous metrics at low S/L behave differently (i.e. ΔPO_4 low S/L, SBF is negatively associated with spicule density at 35 days, $\rho = -0.505$,

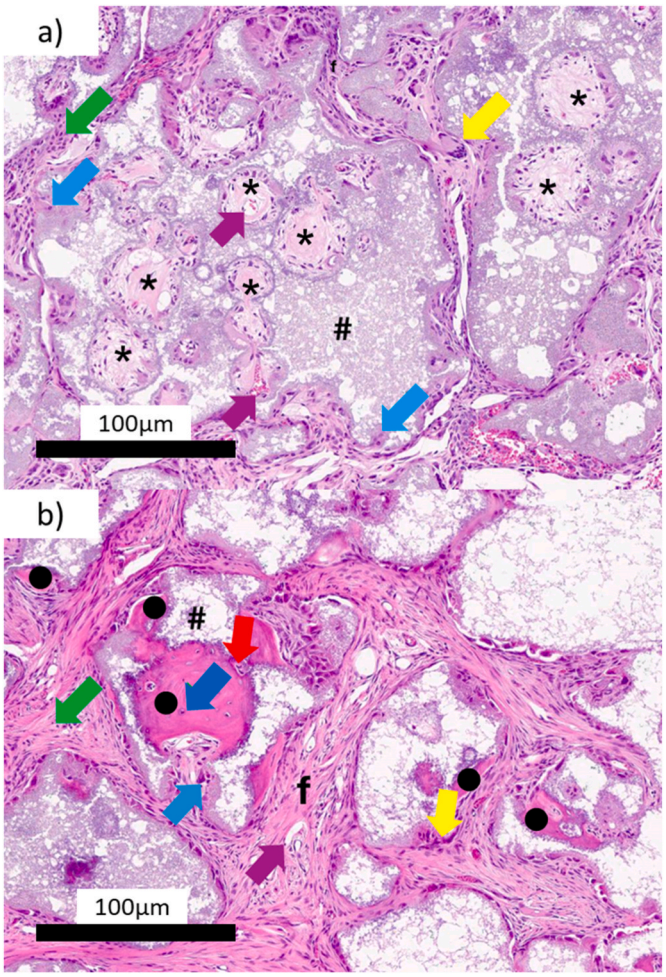

Fig. 11. a) Example of the different cell populations and histological features at 35D in TA4: Early-stage ossification centers (ESOC, Mesenchymal) (*), Implanted Article (#), Fibrosis/Fibroplasia (f), Giant cells (Yellow arrow), Macrophages (Blue arrow), Lymphocytes (Green arrow); b) Example of the different cell populations and histological features at 56 D in TA4: Late stage ossification centers (LSOC, Woven bone) (●), Implanted Article (#), Fibrosis/Fibroplasia (f), Osteocytes (Dark Blue arrow), Osteoblasts (Red arrow), Giant cells (Yellow arrow), Macrophages (Light Blue arrow), Purple (Neovascularization), Lymphocytes (Green arrow). Abbreviations: TA = non-commercial test material prototypes (labeled TA1–TA4); CN = cyclOs (Mathys Ltd); CP = MagnetOs (Kuros Biosciences); BGS = bone graft substitute; CaP = calcium phosphate. (For interpretation of the references to colour in this figure legend, the reader is referred to the Web version of this article.)

$p = 0.033$) reinforces that the link between chemistry and MIHO is context-dependent; what matters is not bulk solubility in water but the ionic history the material drives in a small volume of physiologically relevant liquid.

Phase fractions appear in the matrix largely as a proxy for the chemistry those phases create once implanted. In this dataset, α-TCP (a phase that readily hydrolyses to CDHA in physiological fluids) content is the single most connected variable, positively associated with ESOC 35 days ($\rho = 0.601$, $p = 0.008$), ESOC 56 days ($\rho = 0.651$, $p = 0.003$), spicule density 35 days ($\rho = 0.515$, $p = 0.029$), spicule density 56 days ($\rho = 0.687$, $p = 0.0016$), and BA/TA 56 days ($\rho = 0.709$, $p = 0.0010$), and negatively associated with polymorphonuclear cells (PMN, Fig. 10) at both 35 days ($\rho = -0.585$, $p = 0.0107$) and 56 days ($\rho = -0.641$, $p = 0.0042$). HA content also shows positive associations at 56 days (ESOC: $\rho = 0.805$, $p = 0.0003$; spicule density: $\rho = 0.669$, $p = 0.006$; BA/TA: $\rho = 0.652$, $p = 0.0085$), whereas β-TCP content is negatively related to the same late readouts (spicule density: $\rho = -0.678$, $p = 0.0020$; BA/TA: $\rho = -0.622$, $p = 0.0059$). These signals should be interpreted for what they really are: they almost certainly reflect the specific interfacial hydrolysis environments (and pore architectures) that co-occur with those chemistries in this panel rather than a universal ranking of intrinsic "solubility." In that spirit, the immune readouts add a useful nuance: tapped density is negatively associated with PMN at 56 days ($\rho = -0.658$, $p = 0.003$), suggesting that tighter packing (smaller intergranular channels) reduces persistent neutrophilic infiltration—an effect that would be expected to favor consolidation in the high-performing constructs.

Two checks argue that the main conclusions are not an artifact. First, the heat map shows "families" of chemically related predictors (e.g., ΔpH in SBF and in BSBF; ΔPO_4 in SBF and in H_2O) lighting up the same late-outcome columns with the same sign, which one would not expect from random noise. Second, repeating the analysis at the material level ($n = 6$, using per-material medians) retains the core signals despite the loss of power: SSA remains positively associated with BA/TA 56 days ($\rho = 0.880$, $p = 0.021$) and spicule density 56 days ($\rho = 0.833$, $p = 0.039$), macroporosity remains negatively associated with both BA/TA 56 days ($\rho = -0.880$, $p = 0.021$) and spicules 56 days ($\rho = -0.833$, $p = 0.039$), and ΔpH (high S/L, BSBF) remains negatively associated with BA/TA 56 days ($\rho = -0.893$, $p = 0.016$) and spicules 56 days ($\rho = -0.845$, $p = 0.034$). That the same triad—high SSA/microporosity, lower macroporosity (more confinement), and stronger acidification at high S/L—survives this harsher test strengthens the inference that these are the robust axes linking features to MIHO in this dataset.

In biological terms, and although the present study did not attempt to make the proper characterizations to conclude on the topic, the correlation that this dataset produces between the acidic phosphate microenvironment and MIHO makes it hard not to speculate that this microenvironment is ideal for osteoclastogenesis [74–76], phenomenon that has been identified as key to MIHO [48,51,77,78].

Finally, without providing a definitive answer, the findings of the present study argue that some physical features sometimes portrayed as end all be all to MIHO such as microporosity, SSA and topography may just be proxies to chemical signals that act in a direct fashion on the biological levers that trigger MIHO. To resolve that question once and for all, only time resolved simultaneous direct measurement of chemical changes within the porosity of BGS on the one hand and cellular/tissue level observation of the biological reaction on the other can provide the evidence necessary to reach a definitive conclusion with regards to the levels of chemical perturbations and elicited inflammatory reaction required to cause MIHO.

5. Conclusion

Across six CaP granule formulations tested in a standardized FVB intramuscular model, MIHO was best predicted by the coupling of curvature-rich pore architecture with a phosphate-driven, mildly acidic interfacial chemistry measured under confined-liquid conditions. Materials that generated acidification of the medium and phosphate release (and thus low Ca/P) at high S/L, most notably TA4, were the only ones to translate this signature into consistent ectopic bone (Figs. 7, 8, and 11) (21/24 sections at 56 days with the highest BA/TA and spicule density), whereas alkaline or largely inert chemistries did not (CN, CP, TA1) and intermediate chemistries produced sporadic bone (TA2, TA3). Micro/nano-textured area (SSA, microporosity) correlated with late consolidation, while intragranular concave macropores correlated with initiation, indicating a hierarchical physical control that focuses and sustains the effective chemistry in small pore volumes. These findings argue that commonly cited physical descriptors (e.g., "high SSA") are most informative when interpreted as enablers of the decisive chemical state and that phase labels primarily matter through the hydrolysis/reprecipitation pathways they engender in physiological buffers. Practically, designing CaP BGS with concave pore networks and persistent submicron texture, and screening them for $\Delta pH/\Delta PO_4$/Ca-to-P at high

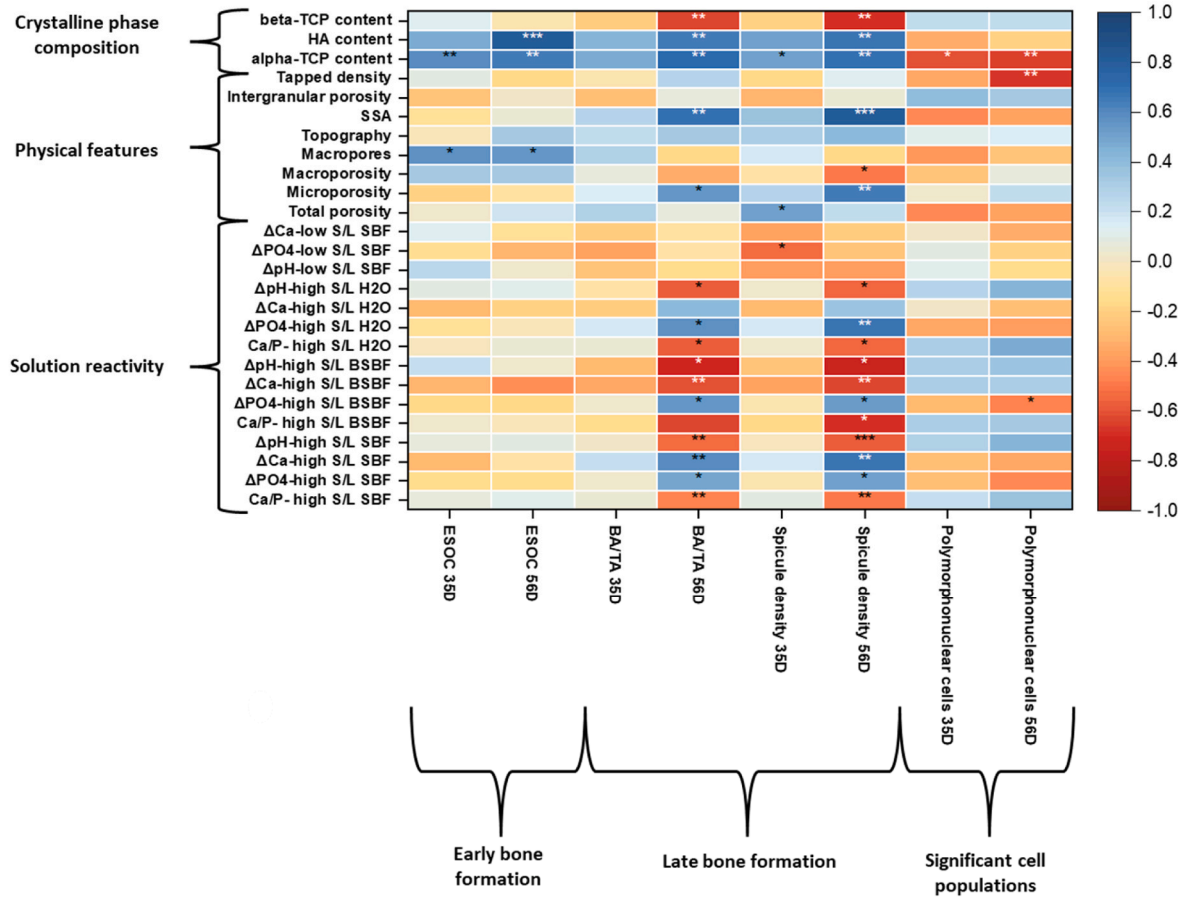

Fig. 12. –Heatmap correlation matrix of Spearman's rank correlation coefficient (ρ) and associated *p* values calculated between physical material descriptors and chemical predictors (Y-axis) and MIHO outcomes (X-axis). Color indicates the direction and magnitude of ρ (blue: positive correlation; red: negative correlation). Statistical significance is indicated as $p < 0.05$ (*), $p < 0.01$ (**), and $p < 0.001$ (***). Abbreviations: ρ, Spearman's rank correlation coefficient; *p*, p value; SSA, specific surface area; Δ, change relative to the corresponding baseline/initial value; Ca, calcium concentration in solution; PO_4, inorganic phosphate concentration in solution; Ca/P, calcium-to-phosphate molar ratio in solution; pH, negative logarithm of hydrogen ion activity; S/L, solid-to-liquid ratio; SBF, simulated body fluid; H_2O, ultrapure/deionized water; BSBF, CO_2/HCO_3^--buffered simulated body fluid (SBF-JL2); ESOC, early-stage ossification centers; BA/TA, bone area over total tissue area; D, days post-implantation. TA = non-commercial test material prototypes (labeled TA1–TA4); CN = cyclOs (Mathys Ltd); CP = MagnetOs (Kuros Biosciences); BGS = bone graft substitute; CaP = calcium phosphate. (For interpretation of the references to colour in this figure legend, the reader is referred to the Web version of this article.)

S/L, offers a rational route to engineer and forecast MIHO performance; future work should pair in-pore, time-resolved chemical mapping with concurrent tissue readouts to establish causality.

CRediT authorship contribution statement

Y. Maazouz: Conceptualization, Data curation, Formal analysis, Funding acquisition, Investigation, Methodology, Project administration, Supervision, Validation, Visualization, Writing – original draft, Writing – review & editing. **F. El Harouni:** Investigation, Visualization. **J. Piot:** Data curation, Investigation. **N. Warfing:** Data curation, Formal analysis. **R. De Miguel:** Conceptualization, Data curation, Formal analysis, Investigation, Visualization. **N. Döbelin:** Conceptualization, Data curation, Supervision, Validation. **M. Bohner:** Conceptualization, Funding acquisition, Investigation, Project administration, Resources, Supervision, Validation, Writing – review & editing.

Declaration of competing interest

The authors declare not to have any conflict of interest regarding the present study. The company Mathys Ltd which provided commercial and noncommercial BGS has chosen to terminate their bone graft substitute business in 2021 and has no commercial nor any other interests in the publication of the present study.

Acknowledgements

The authors would like to thank the swiss funding agency Innosuisse that funded part of this work through the grant 52851.1 IP-LS and the company Mathys Ltd for providing the BGS.

Appendix A. Supplementary data

Supplementary data to this article can be found online at https://doi.org/10.1016/j.mtbio.2026.102918.

Data availability

Data will be made available on request.

References

[1] R.M. Pearce, Notes on the later stages of the repair of kidney tissue (dog) with special reference to pro-liferation of the pelvic epithelium and hetero-plastic bone formation, J. Med. Res. 20 (1909) 53–66.1.

[2] R.W. Selle, M.R. Urist, Calcium deposits and new bone formation in muscle in rabbits, J. Surg. Res. 1 (1961) 132–141, https://doi.org/10.1016/S0022-4804(61)80010-3.

[3] M.R. Urist, B.F. Silverman, K. Büring, F.L. Dubuc, J.M. Rosenberg, The bone induction principle, Clin. Orthop. 53 (1967) 243–283.

[4] M.R. Urist, T.A. Dowell, P.H. Hay, B.S. Strates, Inductive substrates for bone formation, Clin. Orthop. 59 (1968) 59–96.

[5] M.R. Urist, Bone: formation by autoinduction, Science 150 (1965) 893–899.

[6] K.A. Van de Putte, M.R. Urist, Osteogenesis in the interior of intramuscular implants of decalcified bone matrix, Clin. Orthop. 43 (1965) 257–270, https://doi.org/10.1097/00003086-196500430-00026.

[7] F.L. Dubuc, M.R. Urist, The accessibility of the bone induction principle in surface-decalcified bone implants, Clin. Orthop. 55 (1967) 217–223.

[8] M.R. Urist, B.S. Strates, Bone morphogenetic protein, J. Dent. Res. 50 (1971) 1392–1406.

[9] J.H. Heinen Jr., G.H. Dabbs, H.A. Mason, The experimental production of ectopic cartilage and bone in the, J. Bone Joint Surg. Am. 31 (A) (1949) 765–775, https://doi.org/10.2106/00004623-194931040-00007.

[10] J.B. Bridges, J.J. Pritchard, Bone and cartilage induction in the rabbit, J. Anat. 92 (1958) 28–38.

[11] N.A. Mignemi, M. Yuasa, C.E. Baker, S.N. Moore, R.C. Ihejirika, W.K. Oelsner, C. S. Wallace, T. Yoshii, A. Okawa, A.S. Revenko, J.M. Cates, J.G. Schoenecker, Plasmin prevents dystrophic calcification after muscle injury, J. Bone Miner. Res. 32 (2017) 294–308, https://doi.org/10.1002/jbmr.2973.

[12] S.N. Moore-Lotridge, Q. Li, B.H.Y. Gibson, J.T. Martin, G.D. Hawley, T.H. Arnold, M. Saito, S. Tannouri, H.S. Schwartz, R.J. Gumina, J.M.M. Cates, J. Uitto, J. G. Schoenecker, Trauma-induced nanohydroxyapatite deposition in skeletal muscle is sufficient to drive heterotopic ossification, Calcif. Tissue Int. 104 (2019) 411–425, https://doi.org/10.1007/s00223-018-0502-5.

[13] C. Meyers, J. Lisiecki, S. Miller, A. Levin, L. Fayad, C. Ding, T. Sono, E. McCarthy, B. Levi, A.W. James, Heterotopic ossification: a comprehensive review, JBMR Plus 3 (2019) e10172, https://doi.org/10.1002/jbm4.10172.

[14] G.J. Linden, Bone induction in implants of decalcified bone and dentine, J. Anat. 119 (1975) 359–367.

[15] G.D. Winter, B.J. Simpson, Heterotopic bone formed in a synthetic sponge in the skin of young pigs, Nature 223 (1969) 88–90.

[16] M.E. Nimni, S. Bernick, D.T. Cheung, D.C. Ertl, S.K. Nishimoto, W.J. Paule, C. Salka, B.S. Strates, Biochemical differences between dystrophic calcification of cross-linked collagen implants and mineralization during bone induction, Calcif, Tissue Int. 42 (1988) 313–320, https://doi.org/10.1007/BF02556366.

[17] S. Fujibayashi, M. Neo, H.M. Kim, T. Kokubo, T. Nakamura, Osteoinduction of porous bioactive titanium metal, Biomaterials 25 (2004) 443–450, https://doi.org/10.1016/s0142-9612(03)00551-9.

[18] D. Barbieri, A.J.S. Renard, J.D. de Bruijn, H. Yuan, Heterotopic bone formation by nano-apatite containing poly(D,Llactide) composites, Eur. Cell. Mater. 19 (2010) 252–261.

[19] P. Habibovic, M.C. Kruyt, M. V Juhl, S. Clyens, R. Martinetti, L. Dolcini, N. Theilgaard, C.A. van Blitterswijk, Comparative in vivo study of six hydroxyapatite-based bone graft substitutes, J. Orthop. Res. 26 (2008) 1363–1370.

[20] P. Habibovic, H. Yuan, C.M. van der Valk, G. Meijer, C.A. van Blitterswijk, K. de Groot, 3D microenvironment as essential element for osteoinduction by biomaterials, Biomaterials 26 (2005) 3565–3575.

[21] R. Duan, D. Barbieri, X. Luo, J. Weng, C. Bao, J.D. de Bruijn, H. Yuan, Variation of the bone forming ability with the physicochemical properties of calcium phosphate bone substitutes, Biomater. Sci. 6 (2018) 136–145, https://doi.org/10.1039/C7BM00717E.

[22] A.M.C. Barradas, H. Yuan, C.A. van Blitterswijk, P. Habibovic, Osteoinductive biomaterials: current knowledge of properties, experimental models and biological mechanisms, Eur. Cell. Mater. 21 (2011) 407–429, https://doi.org/10.22203/eCM.v021a31, discussion 429.

[23] M. Bohner, R.J. Miron, A proposed mechanism for material-induced heterotopic ossification, Mater. Today 22 (2019) 132–141, https://doi.org/10.1016/j.mattod.2018.10.036.

[24] Y. Maazouz, I. Rentsch, L. Bin, B.L.G. Santoni, N. Doebelin, M. Bohner, Corrigendum to 'In vitro measurement of the chemical changes occurring within β-tricalcium phosphate bone graft substitutes', Acta Biomater. 102 (2020) 440–457, https://doi.org/10.1016/j.actbio.2021.07.025 (S1742706119307858), (10.1016/j.actbio.2019.11.035)), Acta Biomater. 134 (2021) 818.

[25] Y. Maazouz, G. Chizzola, N. Döbelin, M. Bohner, Cell-free, quantitative mineralization measurements as a proxy to identify osteoinductive bone graft substitutes, Biomaterials 275 (2021) 120912, https://doi.org/10.1016/j.biomaterials.2021.120912.

[26] M. Bohner, Y. Maazouz, M.-P. Ginebra, P. Habibovic, J.G. Schoenecker, H. Seeherman, J.J.J.P. van den Beucken, F. Witte, Sustained local ionic homeostatic imbalance caused by calcification modulates inflammation to trigger heterotopic ossification, Acta Biomater. 145 (2022) 1–24, https://doi.org/10.1016/j.actbio.2022.03.057.

[27] J. Gustavsson, M.P. Ginebra, E. Engel, J. Planell, Ion reactivity of calcium-deficient hydroxyapatite in standard cell culture media, Acta Biomater. 7 (2011) 4242–4252, https://doi.org/10.1016/j.actbio.2011.07.016.

[28] J.-M. Sadowska, J. Guillem-Marti, E.B. Montufar, M. Espanol, M.-P. Ginebra, Biomimetic versus sintered calcium phosphates: the In vitro behavior of osteoblasts and mesenchymal stem cells, Tissue Eng. Part A 23 (2017) 1297–1309, https://doi.org/10.1089/ten.tea.2016.0406.

[29] J.M. Sadowska, J. Guillem-Marti, M. Espanol, C. Stähli, N. Döbelin, M.-P. Ginebra, In vitro response of mesenchymal stem cells to biomimetic hydroxyapatite substrates: a new strategy to assess the effect of ion exchange, Acta Biomater. 76 (2018) 319–332, https://doi.org/10.1016/j.actbio.2018.06.025.

[30] Y. Maazouz, I. Rentsch, B. Lu, B. Le Gars Santoni, N. Doebelin, M. Bohner, In vitro measurement of the chemical changes occurring within β-tricalcium phosphate bone graft substitutes, Acta Biomater. 102 (2020) 440–457, https://doi.org/10.1016/j.actbio.2019.11.035.

[31] Z. Yang, H. Yuan, W. Tong, P. Zou, W. Chen, X. Zhang, Osteogenesis in extraskeletally implanted porous calcium phosphate ceramics: variability among different kinds of animals, Biomaterials 17 (1996) 2131–2137.

[32] H. Yuan, C.A. van Blitterswijk, K. de Groot, J.D. de Bruijn, Cross-Species comparison of ectopic bone Formation, Tissue Eng. 12 (2006) 1607–1615.

[33] B.H. Fellah, O. Gauthier, P. Weiss, D. Chappard, P. Layrolle, Osteogenicity of biphasic calcium phosphate ceramics and bone autograft in a goat model, Biomaterials 29 (2008) 1177–1188, https://doi.org/10.1016/j.biomaterials.2007.11.034.

[34] P. Habibovic, M. van den Doel, C.A. van Blitterswijk, K. de Groot, Performance of osteoinductive biphasic calcium-phosphate ceramic in a critical-sized defect in goats, Key Eng. Mater. 309–311 (2006) 1303–1306.

[35] A.M.C. Barradas, H. Yuan, J. van der Stok, B. Le Quang, H. Fernandes, A. Chaterjea, M.C.H. Hogenes, K. Shultz, L.R. Donahue, C. van Blitterswijk, J. de Boer, The influence of genetic factors on the osteoinductive potential of calcium phosphate ceramics in mice, Biomaterials 33 (2012) 5696–5705, https://doi.org/10.1016/j.biomaterials.2012.04.021.

[36] ASTM F2529 − 13. Standard Guide for in Vivo Evaluation of Osteoinductive Potential for Materials Containing Demineralized Bone (DBM)1, (n.d.).

[37] N. Doebelin, R. Kleeberg, Profex: a graphical user interface for the Rietveld refinement program BGMN, J. Appl. Crystallogr. 48 (2015) 1573–1580, https://doi.org/10.1107/S1600576715014685.

[38] K. Sudarsanan, R.A. Young, Significant precision in crystal structure details: holly springs hydroxyapatite, Acta Crystallogr. B25 (1969) 1534–1543, https://doi.org/10.1107/S0567740869004298.

[39] L.W. Schroeder, B. Dickens, W.E. Brown, Crystallographic studies of the role of Mg as a stabilizing impurity in β-Ca3(PO4)2. II. Refinement of Mg-containing β-Ca3(PO4)2, J. Solid State Chem. 22 (1977) 253–262, https://doi.org/10.1016/0022-4596(77)90002-0.

[40] M. Mathew, L.W. Schroeder, B. Dickens, W.E. Brown, The crystal structure of α-Ca3(PO4)2, Acta Crystallogr. B 33 (1977) 1325–1333, https://doi.org/10.1107/s0567740877006037.

[41] Y. Maazouz, I. Rentsch, B. Lu, B.L.G. Santoni, N. Doebelin, M. Bohner, In vitro measurement of the chemical changes occurring within β-tricalcium phosphate bone graft substitutes, Acta Biomater. 102 (2020) 440–457, https://doi.org/10.1016/j.actbio.2019.11.035.

[42] International Organization for Standardization, ISO 23317:2012 - Implants for Surgery – in Vitro Evaluation for apatite-forming Ability of Implant Materials, ISO, Switzerland, 2012.

[43] M. Bohner, J. Lemaitre, Can bioactivity be tested in vitro with SBF solution? Biomaterials 30 (2009) 2175–2179, https://doi.org/10.1016/j.biomaterials.2009.01.008.

[44] Z. Tang, X. Li, Y. Tan, H. Fan, X. Zhang, The material and biological characteristics of osteoinductive calcium phosphate ceramics, Regen. Biomater. 5 (2018) 43–59, https://doi.org/10.1093/rb/rbx024.

[45] A. Barba, A. Diez-Escudero, Y. Maazouz, K. Rappe, M. Espanol, E.B. Montufar, M. Bonany, J.M. Sadowska, J. Guillem-Marti, C. Öhman-Mägi, C. Persson, M.-C. Manzanares, J. Franch, M.-P. Ginebra, Osteoinduction by foamed and 3D-Printed calcium phosphate scaffolds: effect of nanostructure and pore Architecture, ACS Appl. Mater. Interfaces 9 (2017) 41722–41736, https://doi.org/10.1021/acsami.7b14175.

[46] L.E. Rustom, M.J. Poellmann, A.J. Wagoner Johnson, Mineralization in micropores of calcium phosphate scaffolds, Acta Biomater. 83 (2019) 435–455, https://doi.org/10.1016/j.actbio.2018.11.003.

[47] N.L. Davison, X. Luo, T. Schoenmaker, V. Everts, H. Yuan, F. Barrère-de Groot, J. D. de Bruijn, Submicron-scale surface architecture of tricalcium phosphate directs osteogenesis in vitro and in vivo, Eur. Cell. Mater. 27 (2014) 281–297.

[48] Xpand Biotechnology, Professor Bronkhorstlaan 10 Bldg 48, 3723 MB Bilthoven, The Netherlands, N. Davison, J. Su, H. Yuan, J. Van Den Beucken, J. De Bruijn, F. Barrère-de Groot, Influence of surface microstructure and chemistry on osteoinduction and osteoclastogenesis by biphasic calcium phosphate discs, Eur. Cell. Mater. 29 (2015) 314–329, https://doi.org/10.22203/eCM.v029a24.

[49] R. Duan, L.A. van Dijk, D. Barbieri, F. de Groot, H. Yuan, J.D. de Bruijn, Accelerated bone formation by biphasic calcium phosphate with a novel sub-micron surface topography, Eur. Cell. Mater. 37 (2019) 60–73, https://doi.org/10.22203/ECM.V037A05.

[50] X. Chen, M. Wang, F. Chen, J. Wang, X. Li, J. Liang, Y. Fan, Y. Xiao, X. Zhang, Correlations between macrophage polarization and osteoinduction of porous calcium phosphate ceramics, Acta Biomater. 103 (2020) 318–332, https://doi.org/10.1016/j.actbio.2019.12.019.

[51] N.L. Davison, A.-L. Gamblin, P. Layrolle, H. Yuan, J.D. de Bruijn, F. Barrère-de Groot, Liposomal clodronate inhibition of osteoclastogenesis and osteoinduction by submicrostructured beta-tricalcium phosphate, Biomaterials 35 (2014) 5088–5097, https://doi.org/10.1016/j.biomaterials.2014.03.013.

[52] N.L. Davison, B. ten Harkel, T. Schoenmaker, X. Luo, H. Yuan, V. Everts, F. Barrère-de Groot, J.D. de Bruijn, Osteoclast resorption of beta-tricalcium phosphate controlled by surface architecture, Biomaterials 35 (2014) 7441–7451, https://doi.org/10.1016/j.biomaterials.2014.05.048.

[53] M. Li, X. Guo, W. Qi, Z. Wu, J.D. de Bruijn, Y. Xiao, C. Bao, H. Yuan, Macrophage polarization plays roles in bone formation instructed by calcium phosphate

ceramics, J. Mater. Chem. B 8 (2020) 1863–1877, https://doi.org/10.1039/c9tb02932j.
[54] P. Habibovic, H. Yuan, C.M. Van Der Valk, G. Meijer, C.A. Van Blitterswijk, K. De Groot, 3D microenvironment as essential element for osteoinduction by biomaterials, Biomaterials 26 (2005) 3565–3575, https://doi.org/10.1016/j.biomaterials.2004.09.056.
[55] A. Barba, A. Diez-Escudero, M. Espanol, M. Bonany, J.M. Sadowska, J. Guillem-Marti, C. Öhman-Mägi, C. Persson, M.-C. Manzanares, J. Franch, M.-P. Ginebra, Impact of biomimicry in the design of osteoinductive bone substitutes: nanoscale matters, ACS Appl. Mater. Interfaces 11 (2019) 8818–8830, https://doi.org/10.1021/acsami.8b20749.
[56] F. Shi, X. Fang, T. Zhou, X. Huang, K. Duan, J. Wang, S. Qu, W. Zhi, J. Weng, Macropore regulation of hydroxyapatite osteoinduction via microfluidic Pathway, Int. J. Mol. Sci. 23 (2022) 11459, https://doi.org/10.3390/ijms231911459.
[57] Y. Wu, P. Liu, C. Feng, Q. Cao, X. Xu, Y. Liu, X. Li, X. Zhu, X. Zhang, 3D printing calcium phosphate ceramics with high osteoinductivity through pore architecture optimization, Acta Biomater. 185 (2024) 111–125, https://doi.org/10.1016/j.actbio.2024.07.008.
[58] M. Bianchi, E.R. Urquia Edreira, J.G.C. Wolke, Z.T. Birgani, P. Habibovic, J. A. Jansen, A. Tampieri, M. Marcacci, S.C.G. Leeuwenburgh, J.J.J.P. Van Den Beucken, Substrate geometry directs the in vitro mineralization of calcium phosphate ceramics, Acta Biomater. 10 (2014) 661–669, https://doi.org/10.1016/j.actbio.2013.10.026.
[59] M. Espanol, I. Casals, S. Lamtahri, M.-T. Valderas, M.-P. Ginebra, Assessment of protein entrapment in hydroxyapatite scaffolds by size exclusion chromatography, Biointerphases 7 (2012) 1–10, https://doi.org/10.1007/s13758-012-0037-7.
[60] R.Z. LeGeros, Calcium phosphate-based osteoinductive materials, Chem. Rev. 108 (2008) 4742–4753.
[61] P. Habibovic, T.M. Sees, M.A. van den Doel, C.A. van Blitterswijk, K. de Groot, Osteoinduction by biomaterials–physicochemical and structural influences, J. Biomed. Mater. Res. 77 (2006) 747–762.
[62] H. Yuan, H. Fernandes, P. Habibovic, J. de Boer, A.M. Barradas, A. de Ruiter, W. R. Walsh, C.A. van Blitterswijk, J.D. de Bruijn, Osteoinductive ceramics as a synthetic alternative to autologous bone grafting, Proc. Natl. Acad. Sci. USA. 107 (2010) 13614–13619.
[63] H. Yuan, C.A. Van Blitterswijk, K. De Groot, J.D. De Bruijn, A comparison of bone formation in biphasic calcium phosphate (BCP) and hydroxyapatite (HA) implanted in muscle and bone of dogs at different time periods, J. Biomed. Mater. Res., Part A 78 (2006) 139–147, https://doi.org/10.1002/jbm.a.30707.
[64] H. Yuan, Z. Yang, J.D. De Bruij, K. De Groot, X. Zhang, Material-dependent bone induction by calcium phosphate ceramics: a 2.5-year study in dog, Biomaterials 22 (2001) 2617–2623.
[65] J.M. Sadowska, F. Wei, J. Guo, J. Guillem-Marti, M.P. Ginebra, Y. Xiao, Effect of nano-structural properties of biomimetic hydroxyapatite on osteoimmunomodulation, Biomaterials 181 (2018) 318–332, https://doi.org/10.1016/j.biomaterials.2018.07.058.
[66] C. Drouet, M. Aufray, S. Rollin-Martinet, N. Vandecandelaère, D. Grossin, F. Rossignol, E. Champion, A. Navrotsky, C. Rey, Nanocrystalline apatites: the fundamental role of water, Am. Mineral. 103 (2018) 550–564, https://doi.org/10.2138/am-2018-6415.
[67] L. Bertinetti, C. Drouet, C. Combes, C. Rey, A. Tampieri, S. Coluccia, G. Martra, Surface characteristics of nanocrystalline apatites: effect of Mg surface enrichment on morphology, surface hydration species, and cationic environments, Langmuir 25 (2009) 5647–5654, https://doi.org/10.1021/la804230j.
[68] C. Rey, C. Combes, C. Drouet, S. Cazalbou, D. Grossin, F. Brouillet, S. Sarda, Surface properties of biomimetic nanocrystalline apatites; applications in biomaterials, Prog. Cryst. Growth Charact. Mater. 60 (2014) 63–73, https://doi.org/10.1016/j.pcrysgrow.2014.09.005.
[69] A. Brandao-Burch, J.C. Utting, I.R. Orriss, T.R. Arnett, Acidosis inhibits bone Formation by osteoblasts in vitro by preventing mineralization, calcif, Tissue Int. 77 (2005) 167–174, https://doi.org/10.1007/s00223-004-0285-8.
[70] J. Gustavsson, M.P. Ginebra, J. Planell, E. Engel, Osteoblast-like cellular response to dynamic changes in the ionic extracellular environment produced by calcium-deficient hydroxyapatite, J. Mater. Sci. Mater. Med. 23 (2012) 2509–2520, https://doi.org/10.1007/s10856-012-4705-4.
[71] P. Jin, L. Liu, L. Cheng, X. Chen, S. Xi, T. Jiang, Calcium-to-phosphorus releasing ratio affects osteoinductivity and osteoconductivity of calcium phosphate bioceramics in bone tissue engineering, Biomed. Eng. Online 22 (2023) 12, https://doi.org/10.1186/s12938-023-01067-1.
[72] Y. Zhang, T. Shu, S. Wang, Z. Liu, Y. Cheng, A. Li, D. Pei, The osteoinductivity of calcium phosphate-based biomaterials: a tight interaction with bone healing, Front. Bioeng. Biotechnol. 10 (2022) 911180, https://doi.org/10.3389/fbioe.2022.911180.
[73] X. Lou, D. Huang, G. Li, L. Bai, J. Su, H. Yue, Biomaterials in heterotopic ossification: prophylaxis and promotion, Chem. Eng. J. 497 (2024) 153811, https://doi.org/10.1016/j.cej.2024.153811.
[74] F.L. Yuan, M.H. Xu, X. Li, H. Xinlong, W. Fang, J. Dong, The roles of acidosis in osteoclast biology, Front. Physiol. 7 (2016), https://doi.org/10.3389/fphys.2016.00222.
[75] K. Kato, I. Morita, Acidosis environment promotes osteoclast formation by acting on the last phase of preosteoclast differentiation: a study to elucidate the action points of acidosis and search for putative target molecules, Eur. J. Pharmacol. 663 (2011) 27–39, https://doi.org/10.1016/j.ejphar.2011.04.062.
[76] N.S. Krieger, N.E. Sessler, D.A. Bushinsky, Acidosis inhibits osteoblastic and stimulates osteoclastic activity in vitro, Am. J. Physiol. 262 (1992) F442–F448.
[77] N. Kondo, A. Ogose, K. Tokunaga, H. Umezu, K. Arai, N. Kudo, M. Hoshino, H. Inoue, H. Irie, K. Kuroda, H. Mera, N. Endo, Osteoinduction with highly purified β-tricalcium phosphate in dog dorsal muscles and the proliferation of osteoclasts before heterotopic bone formation, Biomaterials 27 (2006) 4419–4427, https://doi.org/10.1016/j.biomaterials.2006.04.016.
[78] T. Nasu, M. Takemoto, N. Akiyama, S. Fujibayashi, M. Neo, T. Nakamura, EP4 agonist accelerates osteoinduction and degradation of P-tricalcium phosphate by stimulating osteoclastogenesis, J. Biomed. Mater. Res., Part A 89 (2009) 601–608, https://doi.org/10.1002/jbm.a.31984.